Multi-chord spectroscopy during detachment-experiments in Magnum-PSI

Barrois, Rion

Award date:
2017

Multi-chord spectroscopy during detachment-experiments in Magnum-PSI

Master's Graduation Project
Master Science & Technology of Nuclear Fusion
Master Applied Physics

Author:
Rion Barrois

Supervisors:
Wouter Vijvers
Ivo Classen
Roger Jaspers
Richard Engeln

November 20, 2017

TU/e Technische Universiteit Eindhoven University of Technology

DIFFER Dutch Institute for Fundamental Energy Research

Abstract

Fusion energy is generated in extremely hot plasmas, which are confined to the inside of fusion reactors by helical magnetic fields. In the divertor region of these tokamaks, the plasma is in direct contact with the walls of the reactor vessel and, as such, the vessel walls need to withstand heat fluxes that are expected to exceed 20 MW/m^2 in ITER in the absence of any power moderation mechanisms. Dealing with heat fluxes of this magnitude and the corresponding particle fluxes, is one of the major unresolved challenges of fusion research.

Plasma detachment is one of the leading candidates to solve the exhaust challenge. By increasing the neutral density in the region in front of the divertor target, the plasma effectively extinguishes, making the conditions tolerable. However, since plasma detachment is not yet fully understood, experiments are carried out in linear machines such as DIFFER's Magnum-PSI to investigate the processes that play a role during detachment. Moreover, in order to investigate detachment in tokamaks, DIFFER is developing a new multi-spectral imaging diagnostic named MANTIS, which is capable of monitoring the plasma in a 2D and time resolved manner. For the interpretation of MANTIS measurements, emission line ratios need to be converted to plasma parameters, i.e. electron temperatures and electron densities. In case of non-equilibrium plasmas, this requires collisional-radiative (CR) modeling. Yacora, which is such a CR-model for hydrogen plasmas, includes atomic and molecular processes to calculate the population densities for the different excited states. However, before Yacora can be used confidently for plasmas in Magnum-PSI or in actual tokamaks, the model should be validated against experiments. This validation procedure consists of two steps: experimentally determining the excited state population densities and experimentally determining or estimating the ground-state densities of several atomic and molecular species.

As part of this work, a multi-chord spectrometer set-up has been developed and installed on Magnum-PSI. Using its multiple lines-of-sight, the spectrometer is capable of investigating the light that is emitted by the plasma, with a spatial resolution of 1.1 mm. Measurements of radial emission profiles (using an Abel inversion) and the corresponding Boltzmann plots at increasing background pressures show evidence of ionisation, molecular-assisted recombination and electron-ion-recombination to play a role at subsequent stages during the onset of detachment. Additionally, the new spectrometer system is capable of measuring the excited state population densities that are needed to validate Yacora. The actual validation, however, is outside the scope of this project, since this requires a method to determine the ground-state densities of several plasma species, which could not be done during the project.

Contents

Chapter 1

Introduction

1.1 The energy problem

Driven by a steady economic growth and a growing world population, the world-wide consumption of energy is continuously increasing. In fact, the International Energy Agency (IEA) has predicted that the demand for energy will continue to grow by nearly one-third in the period between 2013 and 2040 [1]. Since the availability of energy is key for human well-being and development, it is crucial to guarantee access to energy resources to everyone, meaning that the global energy production needs to be intensified in order to keep up with the demands.

At the moment, fossil fuels, such as coal, oil and gas, are the world's primary source of energy. However, the combustion of these resources raises serious environmental concerns due to the consequent emission of greenhouse gases into our atmosphere, which contribute to global warming and climate change. Moreover, the usage of fossil fuels to keep up with the growing demand for energy is non-sustainable, since the world's resources are steadily being depleted and only coal will be left within 40 years [2].

Therefore, in order to close the energy gap between supply and demand without relying on the availability of fossil fuels, the exploration and development of new, sustainable energy sources, such as solar cells, wind power, biofuels and nuclear fusion, is absolutely essential.

1.2 Nuclear fusion, tokamaks and plasma confinement

Nuclear fusion as a source of energy relies on the merging reaction between two light atomic nuclei. When two of these nuclei have a sufficiently high energy to overcome the repulsive electrostatic Coulomb barrier between them, they can collide with each other, fusing into a heavier particle, while releasing a small amount of energy [3]. Even though a number of different fusion reactions can, in principle, be used for this purpose, the deuterium-tritium fusion reaction, as given by equation 1.1, is considered to be the best candidate for large-scale power generation. This is because it is easiest to use, since it has a relatively high reaction rate at relatively low temperatures, as illustrated by figure 1.1.

$$ {}^{2}_{1}\mathrm{D} + {}^{3}_{1}\mathrm{T} \rightarrow {}^{4}_{2}\mathrm{He} + {}^{1}_{0}\mathrm{n} \quad (+\ 17.6\ \mathrm{MeV}) \tag{1.1} $$

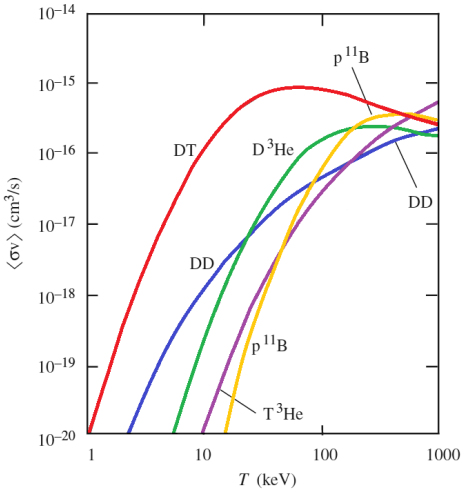

Figure 1.1: An overview of the reaction rates of the most commonly considered fusion reactions as a function of the temperature [4].

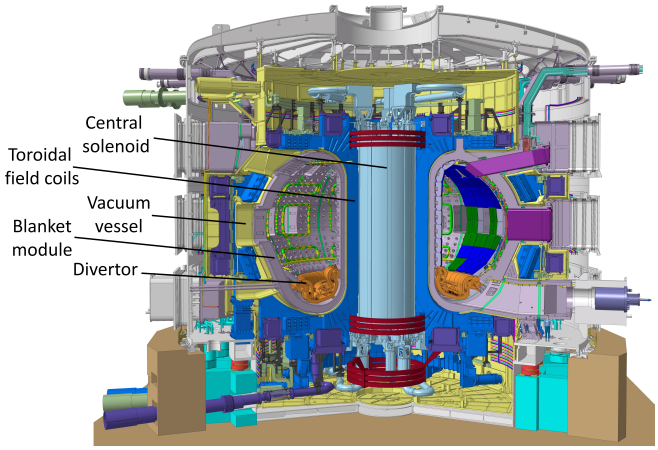

Figure 1.2: A schematic overview of the ITER-reactor, which is currently being build in Caderache, in the south of France, showing its most important components. Credit: ITER Organization, `http://www.iter.org/`.

Figure 1.1 also shows that the reaction rates of different fusion reactions heavily depend on the temperature T. Consequently, a significant amount of external heating is needed to reach the conditions for which thermonuclear fusion becomes self-sustaining. This does not necessarily mean that the temperature should be $T \approx 70$ keV, which is the temperature at which the reaction rate reaches its maximum. In fact, the optimal fusion temperature is at $T \approx 15$ keV or 170 million °C, as the fusion power at this temperature is maximised for a given pressure and the criterion on the triple product of density, temperature and confinement time is easiest to satisfy. In this case, there are enough fusing particles in the tail of the Maxwellian energy distribution to maintain the burning fusion plasma [3].

At these temperatures, the D-T mixture has become an ionised plasma, which needs to be confined to the centre of the fusion reactor to prevent it from damaging the reactor walls, as well as to make sure that the fuel has enough time to take part in fusion reactions [5]. A tokamak, currently the world's leading fusion reactor design, does so by capturing the electrically charged particles of which a plasma consists within a magnetic cage of closed helical field lines. Closed field lines are required to minimize parallel end losses, while the helicity is needed to counteract charge separation due to the so-called $E \times B$-drift and, therefore, for the stability of the magnetic configuration.

Like other tokamaks, the ITER-reactor, which aims to be the first fusion reactor that produces more power than it needs to operate [6], produces its helical field by superimposing a toroidal and poloidal magnetic field. ITER's toroidal field coils, as shown in figure 1.2, are responsible for generating the toroidal magnetic field of which the magnetic field lines circle around the central solenoid in a horizontal plane. At the same time, the central solenoid is used to drive a toroidal current in the plasma, which in turn generates a poloidal magnetic field of which the field lines circle around the plasma in a vertical cross-section of the torus. The combination of both results in the helical field that is used to confine the fusion plasma.

Since transport parallel to the field lines is unaffected by the magnetic fields, particles can move freely along these helical field lines with a parallel velocity $v_{\parallel}$ that is typically comparable to the plasma sound speed c_s. Cross-field transport, on the other hand, is in the classical limit typically the result of particle collisions and, as such, the perpendicular velocity $v_{\perp}$ can be characterised by a perpendicular diffusion coefficient $D_{\perp} \propto \rho_L^2/\tau_c$, in which ρ_L is the gyro-radius and τ_c is the collision time. A comparison between parallel and cross-field transport shows that transport of charged particles is dominant in the direction along the magnetic field lines and, therefore, the plasma is indeed magnetically confined to the helical field lines [7].

1.3 Divertor conditions and scrape-off layer physics

Even though it usually takes numerous rotations through the tokamak parallel to the helical magnetic field lines, the small amount of cross-field transport will eventually cause the particles (and heat) to diffuse outward, i.e. in a radial direction away from the core of the reactor. As soon as the particles cross the outermost (last) closed flux surface (LCFS) or separatrix (as shown in figure 1.3), transport along the magnetic field lines, which is still the preferred transport direction, causes the heat and particles to flow straight towards the divertor region of the tokamak. The small region outside the LCFS in which this parallel transport takes place, is called the scrape-off layer (SOL). Due to the high energy density in the core of the reactor, the heat flux density inside the SOL is enormous, which leads to extreme conditions at the divertor region of the reactor. In the case of ITER, the heat load to the divertor will typically be 10-20 MW/m^2 with transient loads of up to 1 GW/m^2 during Edge Localised Modes (ELMs) [8].

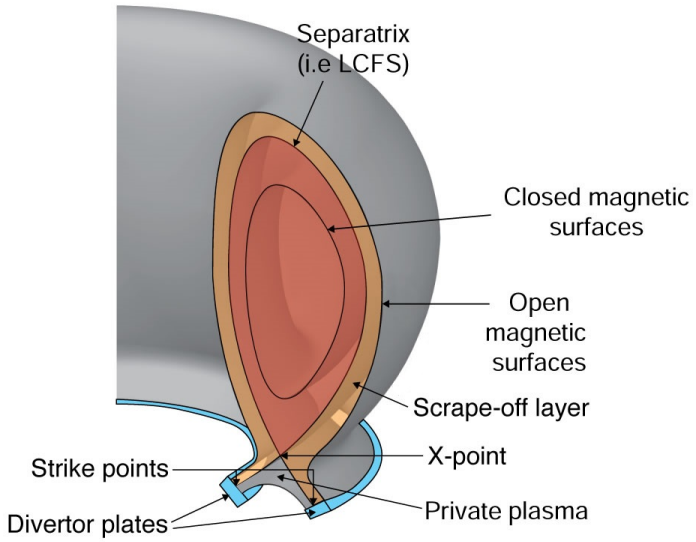

Figure 1.3: A sketch of the tokamak geometry, showing the nested magnetic flux surfaces that make up the magnetic field configuration, as well as the LCFS, the scrape-off layer and the divertor. Credit: United Kingdom Atomic Energy Authority, `https://www.gov.uk/ukaea/`.

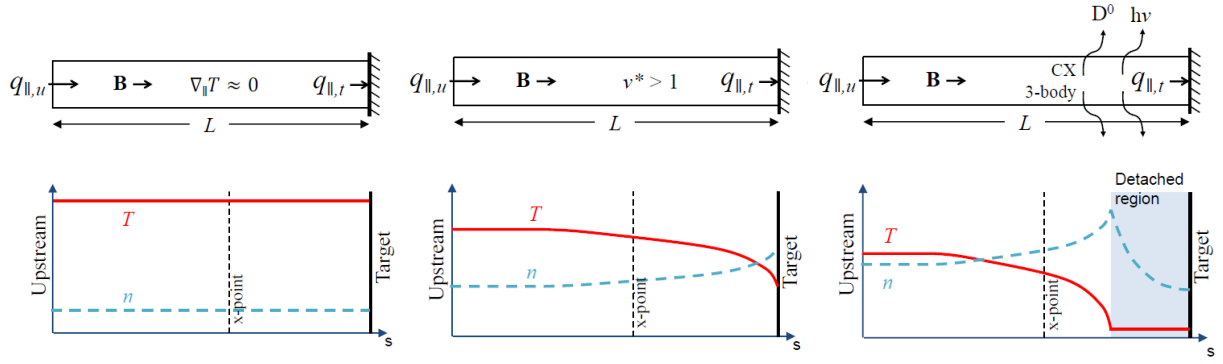

(a) Sheath-limited (attached).

(b) Conduction-limited (high recycling).

(c) Detached.

Figure 1.4: A schematic representation of a straightened out SOL with the main characteristics of the different SOL regime, as well as the typical temperature and density profiles of each regimes as function of the distance to the target [11].

These high thermal heat loads, combined with high plasma particle fluxes and a high neutron fluence, make the conditions in the divertor region extremely challenging for any plasma-facing component (PFC). Materials that are being used as PFC need to have a high melting point and a low sputtering yield. They should be compatible with the plasma and tritium retention should be limited as much as possible. Moreover, the materials have to be able to deal with a constant neutron bombardment without becoming brittle or radioactive. Clearly, it is a rather difficult challenge to find suitable plasma-facing materials that are able to withstand the conditions in the divertor [9]. In fact, the divertor conditions will be even more challenging in DEMO-reactors and future power plants and, therefore, major progress is still needed in dealing with the exhaust of power and particles in fusion reactors [10].

The SOL plays a crucial role in determining the conditions in the divertor region. As mentioned previously, the SOL has to transport heat and particles from the LCFS to the sheath entrance, after which the positively charged sheath region regulates the actual fluxes towards the divertor wall. The heat and particles fluxes entering the SOL, however, cannot be changed, since they are fully dictated by the burning fusion plasma in the core of the reactor, but depending on its operational regime, the SOL can be used to make the conditions less harsh. In general three different SOL regimes are distinguished, as can be seen in figure 1.4: the sheath-limited regime, the conduction-limited regime and the detached regime. Depending on in which regime the divertor is operated, typical values for the plasma parameters that are encountered in the SOL are: $0.1 < T_e < 100$ eV and $10^{18} < n_e < 10^{21}$ m^{-3}.

If the upstream density is relatively small, the SOL plasma is said to be in the sheath-limited regime, which is a regime that is characterized by the absence of large density and temperature gradients along the magnetic field lines. In the case of a sheath-limited SOL, transport is dominated by convection, causing the plasma to flow through the SOL to the sheath entrance along the magnetic field lines without significantly changing its temperature or density. The sheath subsequently acts as a perfect sink and has to exhaust the full inflow of particles and power from the SOL. This operating regime is, therefore, highly undesirable for tokamaks, because of the high plasma temperature at the divertor walls and

the corresponding high sputtering rate.

When the neutral density in the SOL is increased, up to the point that the mean free path λ_{mfp} of neutral particles that are generated at the wall is relatively small in comparison to the connection length of the SOL, the SOL enters the conduction-limited regime. In this regime, the temperature drops towards the wall, whereas the density at the target increases while keeping the total plasma pressure constant. This change of plasma conditions along the magnetic field lines is driven by the continuous chain of recycling: ions recombine at the wall and are released as molecules into the SOL plasma, where they get subsequently dissociated and re-ionised. During these collisional processes, energy is extracted from the hot plasma particles while they are flowing through the SOL. Additionally, the plasma is able to radiate away energy more efficiently at low temperatures and high electron densities, resulting in a strongly radiating region in front of the target. Both the collisional and radiative processes reduce the heat flux towards the divertor wall considerably, making operation in this regime more advantageous than operation in the sheath-limited regime, but it is still not enough to preserve the divertor walls during long pulses [7, 12].

1.4 Plasma detachment

By increasing the neutral density in the SOL even further, the plasma reaches the detached regime (see figure 1.4c). While the density increases, the combined effect of ionisation and radiative cooling will cause the temperature in the SOL to drop below $T_e = 5$ eV. With decreasing temperatures, ionisation becomes less effective, which effectively moves the ion-

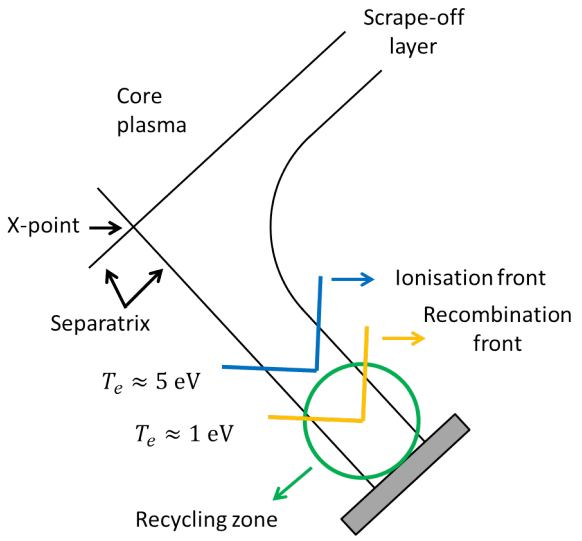

Figure 1.5: A schematic overview of the divertor geometry, showing the different processes that play a role in the onset of detachment, as well as the different regions in which these processes occur.

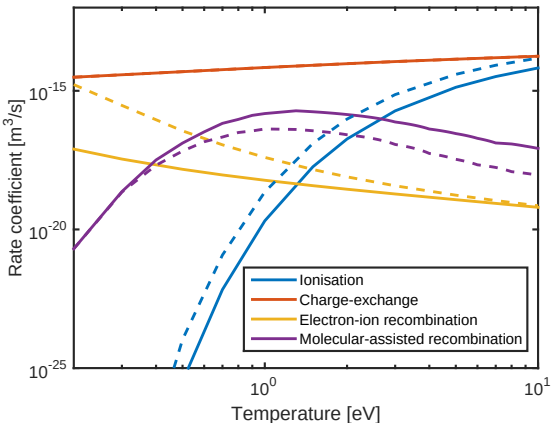

Figure 1.6: The rate coefficients of the different collisional processes that play a role during plasma detachment as function of the temperature T_e for $n_e = 10^{18}$ m^{-3} (solid line) and $n_e = 10^{21}$ m^{-3} (dashed line) [13, 14].

isation region upstream where the temperature is still relatively high (see figure 1.5). At a temperature of 5 eV, the reaction rate for charge-exchange (CX) is significantly larger than the rate for ionisation, as can be seen in figure 1.6. During these CX-collisions, electrons are exchanged between hot plasma ions and relatively cool neutrals, which effectively cools the ions and heats the recycled neutrals. Since only the cooled ions (previously neutral) are confined by the magnetic fields and, thus, directed towards the divertor wall, CX helps in reducing the heat flux towards the divertor. Because the hot particles, which are now neutral, are not trapped by the magnetic field any more, they are allowed to spread through the SOL and lose their momentum to a relatively large surface area. Both consequences of the charge exchange reactions are extremely beneficial in protecting the PFCs.

However, when the temperature decreases below $T_e \approx 2$ eV, either due to the ongoing collisional and radiative processes or due to the increase of the neutral density by actively seeding more neutrals, volumetric recombination processes will start to play a role. These processes can be separated in two categories: molecular-assisted recombination (MAR) and electron-ion recombination (EIR). The first of these processes is most important at temperatures between $0.5 < T_e < 2$ eV (see figure 1.6), and relies on a precursor reaction to convert vibrationally excited hydrogen molecules into ions that take part in the actual recombination reaction. Depending on the temperature and the plasma composition, MAR can manifest itself via either of the following two reaction chains [14]:

$$\mathrm{H}_2(\nu) + \mathrm{e}^- \rightarrow \mathrm{H}^- + \mathrm{H}(1) \;\text{ followed by }\; \mathrm{H}^- + \mathrm{H}^+ \rightarrow \mathrm{H}(1) + \mathrm{H}(p) \tag{1.2}$$

and

$$\mathrm{H}_2(\nu) + \mathrm{H}^+ \rightarrow \mathrm{H}_2^+ + \mathrm{H}(1) \;\text{ followed by }\; \mathrm{H}_2^+ + \mathrm{e}^- \rightarrow \mathrm{H}(1) + \mathrm{H}(p) \tag{1.3}$$

in both reaction chains $\mathrm{H}_2(\nu)$ indicates a vibrationally excited hydrogen molecule with $\nu \geq 4$ [15] (also see appendix A). Moreover, depending on which recombination reaction takes place, table 1.1 shows which excited states are predominantly occupied by the produced excited hydrogen atoms $\mathrm{H}(p)$.

At even lower temperatures, the reaction rate of MAR drops in favour of the rate coefficient for EIR, which is the dominating process at temperatures $T_e \leq 0.5$ (see figure 1.6). The following expression shows the reaction for three-body EIR:

$$\mathrm{H}^+ + \mathrm{e}^- + \mathrm{e}^- \rightarrow \mathrm{H}(p) + \mathrm{e}^- \tag{1.4}$$

in which the excited hydrogen atom preferably occupies the higher excited states (see table 1.1).

Table 1.1: Production mechanisms of excited hydrogen atoms [16], excluding direct excitation.

Name	Reaction	Production of $\mathrm{H}(p)$
Dissociative recombination of H_2^+	$\mathrm{H}_2^+ + \mathrm{e}^- \rightarrow \mathrm{H}(p) + \mathrm{H}(1)$	$n = 2$-4
Atomic mutual neutralisation	$\mathrm{H}^+ + \mathrm{H}^- \rightarrow \mathrm{H}(p) + \mathrm{H}(1)$	$n = 3$
Molecular mutual neutralisation	$\mathrm{H}_2^+ + \mathrm{H}^- \rightarrow \mathrm{H}(p) + \mathrm{H}_2$	$n = 4$-7
Three-body recombination	$\mathrm{H}^+ + \mathrm{e}^- + \mathrm{e}^- \rightarrow \mathrm{H}(p) + \mathrm{e}^-$	$n \geq 6$
Dissociative recombination of H_3^+	$\mathrm{H}_3^+ + \mathrm{e}^- \rightarrow \mathrm{H}(p) + \mathrm{H}_2$	$n = 2$

In either case, ions and electrons recombine into neutrals, not just at the target surface, but in a larger volume near the divertor wall. This leads to a further drop of the electron temperature and density, eventually causing the plasma to extinguish in close proximity to the target. The added disadvantage is that also the upstream conditions may degrade due to the effects of volume recombination [11, 12]. A key characteristic of the detached regime is that the plasma pressure in the SOL drops parallel to the magnetic field lines [17], which effectively decouples the plasma conditions at the target from the ones upstream (see figure 1.4c). At the same time, the strongly radiating region in front of the target will grow [18] and dissipate an even larger fraction of the power flowing towards the divertor wall. As such, plasma detachment is a key solution to lower the heat flux towards the plasma-facing components in tokamaks to an acceptable level [10].

1.5 MANTIS: a multi-spectral 2D imaging diagnostic

In order to study the physics of detachment in tokamak divertors, the Dutch Institute for Fundamental Energy Research (DIFFER) is currently developing a new diagnostic, named MANTIS [19]. MANTIS, which stands for Multi-spectrally Acquiring Narrowband Time-resolved Imaging System, is a real-time 2D imaging diagnostic that uses 10 different cameras to measure the intensity of light emitted by the fusion plasma in 10 narrow pre-determined spectral bands. Figure 1.7 shows a schematic overview of the optical set-up of MANTIS.

Light enters the diagnostic through the relay optics tube at the bottom right of the set-up and an image of the divertor region (or any other plasma that is being observed) is made onto the first mirror (bottom left). After that, the light is reflected back and forth between the mirrors on the left and the dielectric interference filters on the right, each time making a new image on the next mirror. Each of the filters will transmit a small fraction of the light that has a wavelength within specific pre-determined spectral bands. The transmitted light will be imaged onto one of the 10 cameras, which will all simultaneously capture an image

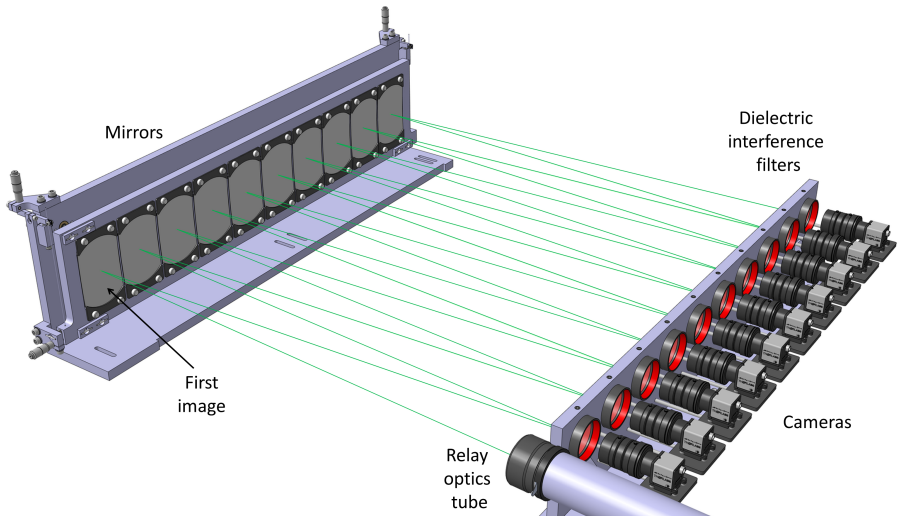

Figure 1.7: A schematic overview of MANTIS, DIFFER's multi-spectral imaging diagnostic. Credit: Dutch Institute for Fundamental Energy Research, `https://www.differ.nl/`.

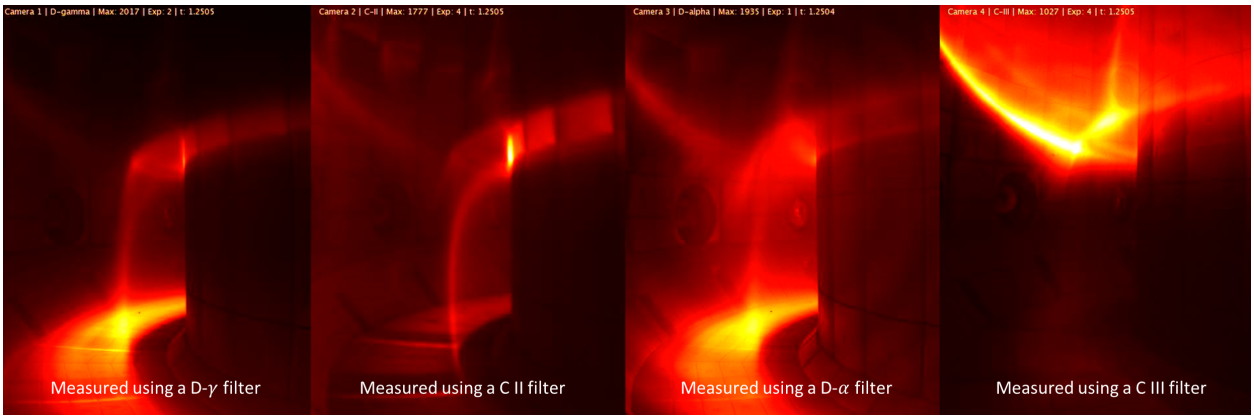

Figure 1.8: Multi-spectral images of the divertor region of the Tokamak à Configuration Variable (TCV) in Lausanne, as taken by the MultiCam set-up. The MultiCam is a four-camera set-up which is the predecessor of MANTIS [20, 21].

of the investigated plasma, similar to the images as shown in figure 1.8.
Some key features of this diagnostic set-up are:

- **Multi-spectral** imaging facilitates the analysis of different plasma processes that play a role in the onset of detachment. Emission in a specific spectral range indicates the presence of certain (excited) plasma species. Moreover, comparisons between different spectral lines, e.g. via line intensity ratios or Boltzmann plots, allow the determination of (population) density ratios and, in case the plasma is in (partial) thermodynamic equilibrium, the electron temperature.
- **Two-dimensional** imaging is needed in order to fully capture the behaviour of divertor plasmas. Inside the LCFS, the plasma properties are constant on each of the nested toroidal flux surfaces, allowing for 1D diagnostics. In tokamak divertors (and linear machines), however, the field lines are open and, as such, plasma parameters can differ in the directions parallel and perpendicular to the magnetic field lines.
- **Real-time** imaging makes it possible to study and control the dynamic behaviour of divertor detachment. As explained in paragraph 1.4, different cooling mechanisms are dominant at different temperatures. While detachment sets in, the different fronts (see figure 1.5) move in the direction along the magnetic field lines and, finally, the degree of detachment can heavily be influenced by time-depending plasma instabilities, such as ELMs (during which the high confinement mode is temporarily lost) or MARFEs (which stands for multifaceted asymmetric radiation from the edge and which describes a situation in which a cold and strongly radiating region is formed near the X-point at the inner edge of the tokamak plasma).

1.6 The Yacora collisional-radiative model

As mentioned before, MANTIS will be used to study the physics of detachment. Key to this investigation is the transformation of the spectral information that MANTIS provides to

2D temperature and density profiles. For certain conditions, plasma equilibria assumptions can be used for this purpose [21]. Unfortunately, these assumptions typically do not hold at all divertor-relevant plasma conditions, i.e. plasmas with an electron density of n_e = 10^{19} - 10^{21} m^{-3} and an electron temperature of T_e = 0.1 - 10 eV. Alternatively, collisional-radiative (CR) modelling can be used to determine the desired plasma parameters from the spectral data gathered by MANTIS.

Yacora, which is such a CR-model for hydrogen, predicts the emission of a plasma by simulating the excitation and de-excitation of hydrogen atoms. In order to do so, the model evaluates the cross-sections of the collisional-radiative processes that occur between the following atomic and, more notably, molecular hydrogen species: H, H^+, H_2, H_2^+, H_3^+ and H^- [22, 23]. Each of the evaluated processes affects the population density of the excited states n_q of the hydrogen atom differently. Therefore, the CR-model calculates so-called population coefficients R_{sq}, which are a function of the electron density and temperature and which are used to quantify the coupling between the different plasma species s and the excited states q. In general, the population density of any excited atomic state (and thus also the total spectrum) can be calculated by multiplying the different population coefficients with the electron density n_e and the quasi-constant ground state densities of the plasma species that are involved in the different collisional-radiative processes.

1.7 Magnum-PSI: DIFFER's linear plasma generator

Linear plasma generators are often utilized to study plasma-surface interactions, scrape-off layer phyiscs and divertor detachment in conditions that are similar to the conditions in actual tokamaks [24]. The open magnetic field lines in linear devices resemble a stretched-

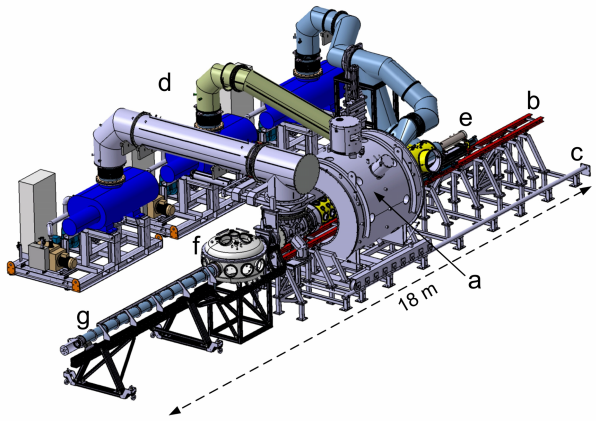

Figure 1.9: A schematic overview of Magnum-PSI, showing the superconducting magnet (a), the roots pumps (d), the cascaded arc source (e) and the target exchange and analysis chamber (f) [25].

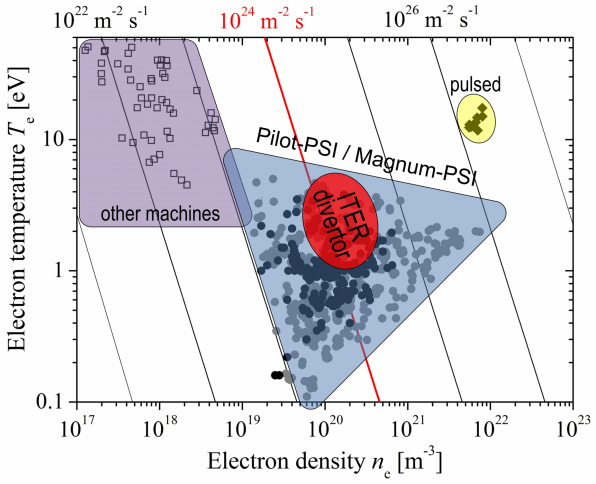

Figure 1.10: The achievable plasma parameters in Magnum-PSI in comparison to the conditions that are expected in ITER and reached in other machines [25].

out version of the magnetic field configuration in the SOL, therefore making these machines quite suitable for research relevant to tokamak divertors. Other advantages of linear machines include better plasma controllability and more access for plasma diagnostics.

DIFFER is home to one of such linear devices: the Magnetized plasma Generator and Numerical Modelling for Plasma Surface Interaction (Magnum-PSI) [25]. A schematic overview of the machine is shown in figure 1.9. Magnum-PSI is capable of reaching plasma conditions that are relevant to the ITER divertor, i.e. plasmas with an electron density of $n_e = 10^{19}$ - 10^{21} m^{-3} and an electron temperature of $T_e = 0.1$ - 10 eV, as can be seen in figure 1.10. Moreover, Magnum-PSI is capable of generating heat fluxes $q > 10$ MW/m^2 and particle fluxes of $\Gamma \approx 10^{23}$ - 10^{25} m^{-2}. In order to do so, the machine uses a cascaded arc source to generate its high density, low temperature plasma [26] and a large 2.5 T superconducting magnet to guide the plasma beam from the source towards the target. Differential pumping inside the vessel guarantees a low neutral background pressure in the target chamber, i.e. $p < 1$ Pa, even when the source is turned on. The relatively low background density indicates that only a very small fraction of the neutrals that are injected at the source are able to reach the target chamber and, therefore, this enables the investigation of neutrals that are released from the target due to recycling. Due to the availability of an additional seeding system that injects a neutral gas into the target chamber, it is also possible to investigate plasma detachment at relatively high background pressures in Magnum-PSI.

Magnum-PSI is equipped with a number of different plasma diagnostics, including: Thomson scattering at the source and target position [27], optical emission spectroscopy (using a 2- and 4-channel Avantes spectrometer) and a fast imaging camera (Phantom V12), which can be used with different spectral filters.

1.8 Multi-chord spectroscopy on Magnum-PSI and report outline

As the Yacora CR-model plays an important role in the interpretation of MANTIS measurements, it is good to experimentally validate Yacora for divertor-relevant plasma conditions, before MANTIS gets installed at the Tokamak à Configuration Variable (TCV) in Lausanne. This validation will be carried out in Magnum-PSI and requires two steps: the calculation of the excited state populations of atomic hydrogen based on the CR-model and the measuring of these populations directly using optical emission spectroscopy.

In order to calculate the excited state population, the ground-state densities of several atomic and molecular hydrogen species (H, H^+, H_2, H_2^+, H_3^+ and H^-) have to be determined, either experimentally or numerically. Subsequently, these ground-state densities need to be multiplied by the electron density and the population coefficients that are calculated by Yacora for the values of T_e and n_e as measured by the Thomson scattering diagnostic, in order to obtain the desired population distribution of the excited states.

This work focuses on the latter of the two validation steps: measuring the excited state populations of atomic hydrogen with optical emission spectroscopy (OES) during detachment experiments on Magnum-PSI. For this purpose, a new multi-chord spectrometer will be installed on Magnum-PSI, which is capable of measuring spatially resolved emission pro-

files and therefore, using an Abel Inversion [54], radial excited state population profiles.

This leads to the following three research questions:

- Is it possible to have detachment in Magnum-PSI, how do the electron temperature, electron density and plasma pressure change during the onset of detachment and is this according to the expectations?
- Is it possible to determine the excited state population density profiles using multi-chord spectroscopy?
- Which processes are responsible for detachment in Magnum-PSI and is it possible to distinguish between these processes by using multi-chord spectroscopy measurements?

In order to answer these questions, experiments have been carried out in Magnum-PSI with the purpose of reaching plasma detachment by gradually increasing the background density in the machine. Meanwhile, the electron temperature and electron density have been measured at different stages during the onset of detachment using the available Thomson scattering diagnostic. This is important, since plasma detachment can be characterised by certain changes in these parameters. At the same time, multi-chord spectroscopy measurements were carried out to obtain the excited state density profiles. Before determining the excited state densities, however, it is useful to consider the different types of plasma radiation, the different line broadening mechanisms and plasma equilibria, since these determine how the measured spectra looks like. Next to that, it is also important to take a look at the basic properties of the multi-chord spectrometer, as these dictate the diagnostic capabilities of the set-up, and the different steps that need to be taken in order to obtain the desired excited state density profiles from the raw data. Finally, the combination of plasma parameters (T_e and n_e) and emission profiles will be used together with the (theoretical) reaction rates of different plasma processes, in order to investigate which process is dominant at which stage during the onset of detachment.

Below, the outline of this thesis is presented by briefly discussing the main topics of each chapter.

Chapter 2: Plasma Radiation Theory

Plasmas are commonly known to emit radiation at different parts of the electromagnetic spectrum, including light in the visible range. This light can be used to diagnose the plasma, since it contains information about the plasma composition, as well as information about the plasma parameters (T_e and n_e). This chapter gives a short summary of the theoretical background, introducing the basic processes (line and continuum radiation) and concepts (line profiles and plasma equilibria) that are of importance when considering optical emission spectroscopy and collisional-radiative modelling.

Chapter 3: Set-up and data analysis

This chapter discusses the multi-chord Jarrell-Ash spectrometer that has been installed

at Magnum-PSI during this project for the purpose of measuring spatially resolved emission profiles and radial excited state population density profiles. In this chapter, the multi-chord spectrometer will be characterised. Additionally, the data analysis chain will be discussed, focusing on the necessary calibration measurements, fitting routines and the utilised Abel inversion method.

Chapter 4: Spectroscopy and detachment experiments in Magnum-PSI

This chapter focuses on the results of the detachment experiments that were carried out in Magnum-PSI. Thomson scattering measurements and Phantom camera images will be presented to show detachment-like behaviour in Magnum-PSI. Subsequently, multi-chord OES measurements at different stages of detachment will be presented. In order to investigate the different processes that play a role during the onset of detachment, radial emission profiles will be shown. Boltzmann plots will be used to investigate whether the plasma is in thermodynamic equilibrium or whether the plasma is ionising or recombining.

Chapter 5: Conclusion and Outlook

The final chapter of this report summarises the main results and discusses the possibilities for follow-up research.

Chapter 2

Plasma radiation theory

This chapter discusses the basics of plasma radiation and plasma spectroscopy, such that this knowledge can be used when analysing the measured spectra. For that reason, line and continuum radiation will be discussed, as well as concepts like spectral line broadening and plasma equilibria. The final paragraph describes the basics of collisional-radiative modeling and the Yacora model.

2.1 Introduction

Plasmas often emit electromagnetic radiation, which can be exploited for the characterisation of these plasmas, i.e. to determine the plasma parameters (T_e and n_e), detect the species that are present or to monitor collisional-radiative processes that take place inside the plasma. In this context, it is useful to make a distinction between three different types of plasma radiation [29], namely:

- **bound-bound emission**, which is the result of the transition of an electron that is bound to an atom (paragraph 2.2) or a molecule (appendix A) from an excited state to a state with a lower energy.
- **free-bound emission** or recombination radiation, which is emitted during a recombination reaction during which a free electron is captured by a positive ion (paragraph 2.4).
- **free-free emission** or Bremsstrahlung, which is emitted when electrons are deflected by the electric fields of other charged plasma particles (paragraph 2.4).

In all these cases, the wavelength λ of the emitted radiation is directly related to the energy of the corresponding photons according to the following equation:

$$\lambda = \frac{hc}{E_{photon}} \tag{2.1}$$

in which c is the speed of light and h is Planck's constant.

In the case of a bound-bound transition, E_{photon} exactly corresponds to the energy difference ΔE between the upper q state and the lower p state between which the transition occurs. As such, the energy of the photon and, therefore, also its wavelength are well-defined:

$$\lambda = \frac{hc}{E_q - E_p} \tag{2.2}$$

Due to the discrete nature of the energy levels of radiating particles (this will be discussed in more detail in paragraph 2.2 and appendix A), a typical bound-bound emission spectrum features a number of characteristic intensity peaks at wavelengths that precisely correspond to the energy differences of possible transitions. As such, these so-called spectral lines are commonly used to identify the radiating species that are present in the plasma.

The intensity of a certain spectral line can be expressed in terms of an emission coefficient ε_{qp} (in W sr^{-1} m^{-3}) at a position r inside the plasma, which is given by the following expression:

$$\varepsilon_{qp}(r) = A_{qp}\frac{h\nu}{4\pi}n_q(r) = A_{qp}\frac{hc}{4\pi\lambda}n_q(r) \tag{2.3}$$

in which A_{qp} is the Einstein coefficient for spontaneous emission corresponding to the specific transition $q \rightarrow p$, while n_q is the population density of the upper energy level q and the frequency of the emitted light is given by $\nu = c/\lambda$.

A spectral emission coefficient (in W sr^{-1} m^{-3} nm^{-1}) can be defined by multiplying line emission coefficients with a line profile $\phi(\lambda)$ that indicates the shape of a spectral line:

$$\varepsilon_{\lambda}^{qp}(r, \lambda) = \varepsilon_{qp}(r)\phi(\lambda) \tag{2.4}$$

Using spectral emission coefficient, it is possible to calculate the so-called spectral radiance L_λ (in W sr^{-1} m^{-2} nm^{-1}) which quantifies the actual spectral power radiated per unit projected area A per solid angle Ω:

$$L_\lambda = \frac{\mathrm{d}^2\Phi_\lambda}{\mathrm{d}A\,\sin\theta\,\mathrm{d}\Omega} = \int \varepsilon_\lambda(s)\,\mathrm{d}s \tag{2.5}$$

in which Φ_λ is the spectral flux (in W/nm), θ is the angle between the normal of the surface element $\mathrm{d}A$ and the direction of the radiation and s is the distance from the surface element $\mathrm{d}A$ to the radiation source.

2.2 Atomic line emission

As mentioned in paragraph 2.1, each line of a bound-bound emission spectrum corresponds to a specific transition of an electron between two energy levels. Therefore, in order to understand such an emission spectrum, one needs to take a close look at the energy level structure of radiating plasma species. This paragraph discusses atomic energy levels, focusing mainly on atomic hydrogen, as well as radiative transitions between these levels.

Bohr's semi-classical atomic model, in which electrons circle around the nucleus of an atom on orbits with different radii, is a good starting point for a discussion about the atomic energy level structure. By balancing the Coulomb force and the centripetal force [30], an expression for the radius of the orbits r can be found as function of the velocity of the electrons v:

$$r = \frac{Ze^2}{4\pi\varepsilon_0 \mu v^2} \tag{2.6}$$

in which Z is the atomic number (or the effective charge of the nucleus), while ε_0 is the vacuum permittivity and μ is the reduced mass of the electron-nucleus system.

Equation 2.6 does not place any restrictions on the radius of the orbits that are possible. However, for any stationary state (the electron should not leave the atom) an exact number of standing de Broglie waves ($\lambda = \lambda_{dB}$) should fit on the circumference of each possible orbit to prevent destructive interference from happening. Therefore, the following condition should also be satisfied:

$$2\pi r = n\lambda_{dB} = n\frac{h}{\mu v} \tag{2.7}$$

in which n is a positive integer. Combining equation 2.6 with equation 2.7 gives an expression for the possible radii of the electron orbits:

$$r_n = \frac{n^2 h^2 \varepsilon_0}{\pi \mu Z e^2} = n^2 \frac{a_0}{Z} \tag{2.8}$$

and their corresponding energies

$$E_n = E_{kin} + E_{pot} = \frac{1}{2}\mu v^2 - \frac{Ze^2}{4\pi\varepsilon_0 r} = -\frac{\mu e^4 Z^2}{8\varepsilon_0^2 h^2 n^2} = -hcR_\infty \frac{Z^2}{n^2} \tag{2.9}$$

in which a_0 denotes the Bohr radius and R_∞ is the Rydberg constant.

From equation 2.9, it is clear that electrons that are bound to the nucleus of an atom can only have certain discrete energy values, each commonly indicated by a principal quantum number n. The ground state, which is the energy level with the lowest energy, is characterised by $n = 1$, excited states are denoted by quantum numbers $n > 1$.

Even though the energy of an atomic state is in Bohr's model completely determined by its principle quantum number n according to equation 2.9, there can be multiple states with the same energy. In order to uniquely differentiate between the different spatial configurations of these degenerate states, one needs to use the additional quantum numbers l for the orbital angular momentum and m for the projection of the orbital momentum onto the z-axis. For a given n, these two quantum numbers can take the following values:

$$l = 0, 1, \ldots, n-1 \qquad\qquad m = 0, \pm 1, \ldots, \pm l \tag{2.10}$$

Based on these conditions for l and m, there are n^2 different degenerate states with an energy E_n that can only be distinguished from each other by indicating them with a combination of all three quantum numbers n, l and m. This degeneracy, however, can be lifted by external fields (the Zeeman-effect), spin-orbit coupling (fine structure splitting) and relativistic effects, leading to the splitting of an energy level into a multitude of different levels which all have a slightly different energy.

For a complete description of the atomic energy level structure, the electrons need to be taken into account as well. The spin of electrons, which is a key property in this context, can

be described in a similar way as the orbital momentum using the quantum numbers s (for the absolute spin value) and m_s (for its projection onto the z-axis). In the case of electrons, the spin of each individual particle is always $s = 1/2$, while m_s can either be $+1/2$ (spin up) or $-1/2$ (spin down). According to Pauli's exclusion principle, each energy level (n, l, m) can in principle be occupied by two electrons, each having a differently oriented spin.

The different electronic states of an atom can now be characterised by a so-called term symbol:

$$n^{2S+1}L_J \tag{2.11}$$

in which n is the atom's principle quantum number, while S is the total spin of the electrons in the unfilled energy levels $S = \sum_i s_i$. L denotes the total orbital angular momentum of the unfilled energy levels $L = \sum_i l_i$, usually indicated by a capital letter: S ($L = 0$), P ($L = 1$), D ($L = 2$), ..., and J is the total electronic angular momentum: $J = L + S$.

The excitation of bound electrons to higher energy levels is governed by collisions between particles or by the absorption of photons. Similarly, de-excitation often goes hand in hand with the emission of a photon that has an energy corresponding to the energy difference between the upper q and lower p energy levels. Not accounting for the relatively small effect of the splitting of degenerate states, equation 2.9 can be used to calculate the photon energy of a bound-bound electron transition for hydrogen and hydrogen-like ions:

$$E_{photon} = E_q - E_p = hcR_\infty Z^2\Big(\frac{1}{p^2} - \frac{1}{q^2}\Big) \tag{2.12}$$

or in terms of a wavelength:

$$\frac{1}{\lambda} = R_\infty Z^2\Big(\frac{1}{p^2} - \frac{1}{q^2}\Big) \tag{2.13}$$

In the case of a hydrogen plasma ($Z = 1$), the emission spectrum consists of a number of spectral series: the Lyman series ($p = 1$) in the ultraviolet, the Balmer series ($p = 2$) in the visible range, the Paschen series ($p = 3$) in the infrared and so on. The different spectral lines in such a series are the direct result of the different upper states $q > p$ that can decay back to the lower energy level p. The wavelength corresponding to each line can be calculated using equation 2.13.

Since this work focuses on spectroscopy in the visible range of the electromagnetic spectrum, we are most interested in the Balmer series. As said before, Balmer lines are the result of the electronic decay of an electron from an excited state q ($q < 2$) to the energy level with $p = 2$. Table 2.1 gives an overview of the characteristics of the most common Balmer lines.

Table 2.1: Properties of the Balmer lines as listed in the NIST atomic database [31].

Name	H-α	H-β	H-γ	H-δ	H-ε	H-ζ	H-η	H-θ
Wavelength (nm)	656.28	486.14	434.05	410.17	397.01	388.91	383.54	379.79
Transition	$3 \to 2$	$4 \to 2$	$5 \to 2$	$6 \to 2$	$7 \to 2$	$8 \to 2$	$9 \to 2$	$10 \to 2$
Einstein Coeff. A_{qp} ($\times 10^5$ s^{-1})	441.01	84.193	25.304	9.7320	4.3889	2.2148	1.2156	0.7123

2.3 Line broadening

2.3.1 Line broadening mechanisms

Although the wavelength of a spectral line is precisely defined in theory, there are several processes that contribute to broaden a spectral line into a distribution $\phi(\lambda)$ with a full width at half maximum (FWHM) $\Delta\lambda$ around the central wavelength λ_0. In general, these broadening mechanisms can be divided in four main categories [29]:

- **Doppler line broadening** is the direct result of the Doppler effect which describes how the wavelength of the emitted radiation gets slightly shifted depending on the motion of the radiating plasma particles with respect to the observer/detector. When assuming the plasma to be in thermodynamic equilibrium (see paragraph 2.5), the velocity distribution of the plasma particles is Maxwellian. The Doppler effect then results in a Gaussian line profile with a FWHM that is proportional to the temperature of the radiating species T_a [29]:

$$\delta\lambda_{dop} = \lambda_0 \sqrt{8\,\ln(2)\,\left(\frac{k_b T_a}{m_a c^2}\right)} \tag{2.14}$$

  in which k_b is the Boltzmann's constant, m_a is the mass of the radiating species and c is the speed of light.

- **Pressure line broadening** is caused by the interactions of a radiating particle with its close neighbours. Depending on the nature of these neighbours, different types of interactions, e.g. inelastic collisions, coulomb interactions and dipole resonances, contribute to the pressure broadening mechanism. Even though, at first, all these processes may seem different, all of them result in Lorentzian line profiles with a FWHM that scales with the density n of the involved plasma species.

  During an inelastic collision with a neutral particle, for instance, the Van der Waals force affects the energy levels of the radiator, leading to Van der Waals broadening of spectral lines with a FWHM as given by the following expression [32]:

$$\delta\lambda_{vdw} = 8.08\,\frac{\lambda^2}{2\pi c}\,v^{3/5}\,C_6^{2/5} N_g \tag{2.15}$$

  in which C_6 is the Van der Waals constant, N_g is the density of the neutral perturbers that can be calculated using the ideal gas law: $N_g = p_{bg}/k_b T_g$, and v is the mean relative velocity that can be calculated using the reduced mass μ of the radiator-perturber system: $v = \sqrt{8k_b T_g/(\pi\mu)}$. The following expression can be used to calculate C_6 [29, 33]:

$$C_6 \approx \frac{e^2}{4\pi\varepsilon_0\hbar}\,\alpha\langle R_i^2\rangle = \frac{e^2}{4\pi\varepsilon_0\hbar}\,\alpha a_0^2\left[\frac{n_i^{*2}}{2}\big(5n_i^{*2} + 1 - 3l_i(l_i+1)\big)\right] \tag{2.16}$$

  in which ε_0 is the vacuum permittivity, $\hbar$ is the reduced Planck constant, α is the polarizability of the neutral perturber, $\langle R_i^2\rangle$ is the mean radius of the emitting atom

in state i (holds for both states of a radiative transition), a_0 is Bohr's radius, n_i^* is the effective quantum number of the radiating atom and l_i is the corresponding angular momentum quantum number. The effective quantum number is given by $n_i^* = E_H/(E_{IP} - E_i)$, in which E_H is the ionization potential of hydrogen, E_{IP} the ionization potential of the radiating atom and E_i the energy of the atomic state i.

Resonance broadening plays a role during interactions between atoms of the same kind when either of the energy level of the radiating transition is resonantly coupled to the ground state g by a dipole transition. The resulting line broadening is characterised by the following FWHM [34]:

$$\delta\lambda_{res} = 3.84\ \lambda^2 \sqrt{\frac{g_g}{g_p}} \frac{e^2 f_R \lambda_R}{16\pi^2 \varepsilon_0 m_e c^2} N_g \tag{2.17}$$

in which e is the electron charge, m_e is the electron mass, λ_R is the wavelength corresponding to the resonant transition, f_R is the corresponding oscillator strength, N_g is the density of ground-state atoms and g_g and g_p are statistical weights.

A third pressure broadening mechanism is driven by Coulomb interactions between charged particles (ions and electrons) and radiating atoms. This processes is called Stark broadening and the resulting FWHM is given by the following expression [29,35]:

$$\delta\lambda_{stark} = 13.7\ \frac{\lambda^2}{2\pi c}\ \frac{\hbar}{m_e} \frac{z}{Z} (n_q^2 - n_p^2) n_z^{3/2} \tag{2.18}$$

in which Z and z are the atomic numbers of respectively the radiator and perturber, n_q and n_p are the quantum numbers corresponding to the radiative transition $q \to p$ and n_z is the density of perturbers.

- **Natural line broadening** originates from the finite lifetime of the excited state. According to Heisenberg's time-energy uncertainty principle, a short-lived (small Δt) excited state cannot have a very precisely defined energy (ΔE is relatively large):

$$\Delta t \cdot \Delta E \geq \frac{\hbar}{2} \tag{2.19}$$

Natural line broadening affects both energy levels of a radiative transition $q \to p$, unless p is the ground state, making the line resemble a Lorentizan profile with the following FWHM:

$$\delta\lambda_{nat} = \frac{\lambda^2}{2\pi c} \Big(\frac{1}{\tau_p} + \frac{1}{\tau_q} \Big) \tag{2.20}$$

in which $1/\tau_i = \sum_j A_{ij}$ is the lifetime of a certain state i, which can be calculated by evaluating the sum of all Einstein coefficient for spontaneous emission of all possible transitions $i \to j$ with $j < i$.

- **Instrumental line broadening** can be attributed to imperfections in the spectrometer set-up, such as the use of non-ideal optics, the axial divergence of monochromatic light, small misalignments in the optical set-up and, maybe most importantly, the actual size of the incoming beam of light due to the finite-sized opening of the entrance slit of the spectrometer. The broadening due to all these effects combined, is measured as the Gaussian instrument function of the spectrometer (see paragraph 3.3).

2.3.2 Voigt profiles

In the previous paragraph, different line broadening mechanisms were discussed, each of them having either a Gaussian ϕ_G or a Lorentzian ϕ_L character with a certain position λ_0 and a certain width $\Delta\lambda$. These corresponding profiles are given by:

$$\phi_G(\lambda, \Delta\lambda) = \sqrt{\frac{4\ \ln(2)}{\pi}} \frac{1}{\Delta\lambda_G} \exp\Big[-4\ \ln 2\ \Big(\frac{\lambda - \lambda_0}{\Delta\lambda_G}\Big)^2 \Big] \tag{2.21}$$

$$\phi_L(\lambda, \Delta\lambda) = \frac{1}{\pi} \frac{\Delta\lambda_L/2}{(\lambda - \lambda_0)^2 + (\Delta\lambda_L/2)^2} \tag{2.22}$$

in which the combined Gaussian half-width $\Delta\lambda_G$ is given by combining the different Gaussian broadening processes in the following way: $(\Delta\lambda_G)^2 = \sum_i (\delta\lambda_{G,i})^2$. Similarly, the combined Lorentzian half-width $\Delta\lambda_L$ can be obtained, using: $\Delta\lambda_L = \sum_i \delta\lambda_{L,i}$.

The actual line profile can be obtained by the convolution of equation 2.21 and equation 2.22. The result is a so-called Voigt profile (see figure 2.1a):

$$\begin{aligned} \phi_V(\lambda, \Delta\lambda_G, \Delta\lambda_L) &= \phi_G(\lambda, \Delta\lambda_G) * \phi_L(\lambda, \Delta\lambda_L) \\ &= \frac{a}{\Delta\lambda_G} \frac{2\ \ln(2)}{\pi^{3/2}} \int_{-\infty}^{\infty} \frac{\exp(-t^2)}{a^2\ \ln(2) + \Big[2\sqrt{\ln(2)}\ \big(\frac{\lambda - \lambda_0}{\Delta\lambda_G}\big) - t\Big]^2}\ \mathrm{d}t \end{aligned} \tag{2.23}$$

in which $a = \Delta\lambda_L/\Delta\lambda_G$ indicates the relative importance of either the Gaussian or Lorentzian part and t is a dummy variable used during the convolution.

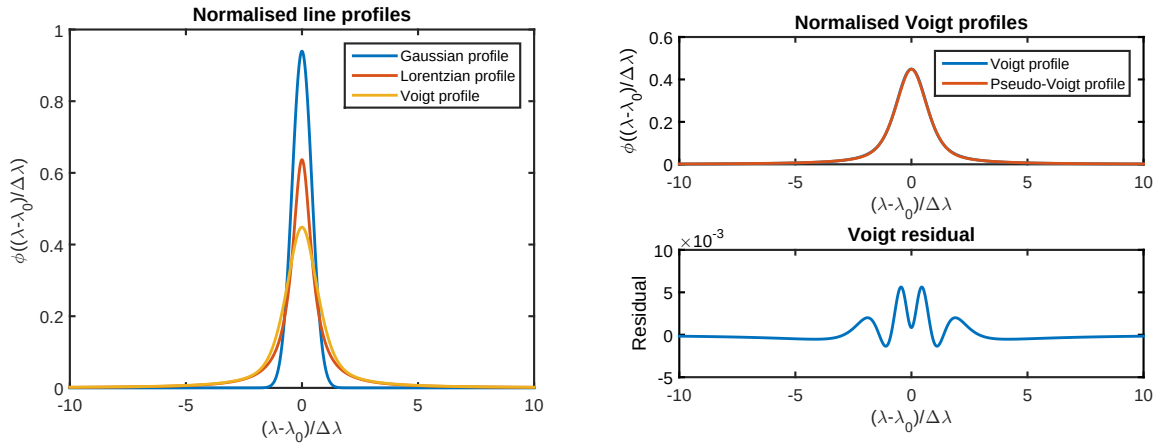

(a) The Voigt profile and its components.

(b) The pseudo-Voigt profile as alternative.

Figure 2.1: The convolution of a Gaussian profile and a Lorentzian profile (both having a halfwidth of 1 in this example) results in a Voigt profile. The Voigt profile can be approximated by a pseudo-Voigt with a discrepancy between both curves within 1% of the peak value. The shown profiles are centered and normalised such that area underneath the profile equals one.

However, because it is rather expensive to calculate the Voigt-convolution from a computational point of view, it is useful to approximate the Voigt function with a pseudo-Voigt profile $\phi_{V'}$, which can directly be obtained from a simple linear combination of ϕ_G and ϕ_L [36]:

$$\phi_{V'}(\lambda, \Delta\lambda_G, \Delta\lambda_L) = \eta\phi_L(\lambda, f) + (1-\eta)\phi_G(\lambda, f) \tag{2.24}$$

with a shape factor η:

$$\eta = 1.36603\ (\Delta\lambda_L/f) - 0.47719\ (\Delta\lambda_L/f)^2 + 0.11116\ (\Delta\lambda_L/f)^3 \tag{2.25}$$

and a halfwidth f:

$$f = \Big(\Delta\lambda_G^5\ +\ 2.69269\ \Delta\lambda_G^4\ \Delta\lambda_L\ +\ 2.42843\ \Delta\lambda_G^3\ \Delta\lambda_L^2\ + \\ 4.47163\ \Delta\lambda_G^2\ \Delta\lambda_L^3\ +\ 0.07842\ \Delta\lambda_G\ \Delta\lambda_L^4\ +\ \Delta\lambda_L^5\Big)^{1/5} \tag{2.26}$$

As can be seen in figure 2.1b, the pseudo-Voigt profile resembles the actual Voigt profile quite good with a discrepancy between both curves within 1% of the peak value.

All previously mentioned line profiles $\phi(\lambda)$ are normalised, meaning that the total area bound by the line profiles and the λ-axis equals 1. As a result of this normalisation, the line profiles can easily be multiplied by the total line emission coefficient $\varepsilon_{qp}(r)$ to obtain its spectral distribution (see equation 2.4).

2.4 Continuum radiation

As mentioned in paragraph 2.1, not all radiation is emitted at very specific wavelengths. In contrast to line radiation, free-bound radiation and free-free radiation emit light in a broad spectrum. The main reason for this is that either the energy of the upper or the lower state of the radiative transition (or both) is unconstrained by a predefined discrete energy level and can take any value.

2.4.1 Recombination radiation

In the case of recombination reactions, a free electron with an initial energy E_{kin} is captured by an ion and together they recombine into a neutral. In the case of three-body recombination, the excess energy is released as kinetic energy of the secondary electron (see equation 1.4). In the case of radiative recombination, the excess energy is emitted as free-bound radiation. The energy of such a recombination photon is then given by:

$$E_q^{fb} = hc/\lambda = E_{kin} + (E_\infty - E_q) = \frac{1}{2}mv^2 + (E_\infty - E_q) \tag{2.27}$$

in which E_q is the energy of an excited state q in which the electron ends up after recombination, as given by equation 2.9, whereas E_∞ is the ionisation energy. The difference between both energies, $E_\infty - E_q$, indicates the amount of energy that is needed for an electron to escape from a given energy level up to the ionisation limit or, in terms of recombination, the binding energy that is released when an electron gets captured by an ion.

Because the initial kinetic energy of the electrons will generally be distributed according to a distribution function, the plasma contains slow electrons as well as fast ones. Due to the continuous behaviour of E_{kin}, E^{fb} can in principle take almost any value, resulting in a continuous free-bound emission spectrum. The discrete energy level structure of the ion, however, is the source of discontinuities in this spectrum. Irrespectively of E_{kin}, the energy of the emitted free-bound photons, as given by equation 2.27, has a lower limited depending on the excited state that is involved during the recombination process. This implies that recombination into an excited state q does not lead to radiation with $\lambda < hc/(E_\infty - E_q)$. Consequently, the actual free-bound emission spectrum shows an edge structure with a number of sharp thresholds at positions that correspond to the energy of the different excited states, as can be seen in figure 2.2a.

Similar to equation 2.3, the free-bound spectral emission coefficient is given by the following equation:

$$\varepsilon_{fb} = \varepsilon_\lambda^{fb}(\lambda)\mathrm{d}\lambda = \sum_{n_q} \frac{hc}{4\pi\lambda} \frac{\mathrm{d}R_q^{rec}}{\mathrm{d}v}\, \mathrm{d}v \tag{2.28}$$

in which R_q^{rec} denotes the recombination reaction rate of free-bound transitions as given in equation 2.29, representing the number of recombination events into an excited state q per unit of time per unit of volume due to collisions between ions (n_Z) and free electrons (n_e) with a kinetic energy E_{kin}. The sum over the principal quantum numbers n_q is needed to include the contributions of the different excited states to the free-bound continuum.

The recombination rate is given by the following equation:

$$\frac{\mathrm{d}R_q^{rec}}{\mathrm{d}v}\mathrm{d}v = n_e n_Z \frac{dk_q^{rec}}{dv} dv = n_e n_Z v f_m(v) \sigma_{E_{kin}\to q}^{rec}\, \mathrm{d}v \tag{2.29}$$

in which k_q^{rec} is the reaction rate coefficient, which is obtained by averaging the recombination cross-section $\sigma_{E_{kin}\to q}^{rec}$ over the Maxwellian velocity distribution $f_m(v)$ of the reacting species:

$$f_m(v) = \Big(\frac{m}{2\pi k_b T_e}\Big)^{3/2} 4\pi v^2 \, \exp\Big(-\frac{mv^2}{2k_b T_e}\Big) \tag{2.30}$$

The cross-section $\sigma_{E_{kin}\to q}^{rec}$ for recombination into an excited state q is given by the following expression:

$$\sigma_{E_{kin}\to q}^{rec} = \frac{2n_q^2}{2m_e c^2} \frac{(h\nu)^2}{\frac{1}{2}m_e v^2} \left[\frac{64\alpha Z^4}{3\sqrt{3}n_q^5}\Big(\frac{E_R}{h\nu}\Big)^3 \pi a_0^2\right] G_q^{bf}(\lambda) \tag{2.31}$$

in which the term between the square brackets is Kramers' classical cross-section for photo-ionisation (Kramers uses cgs units) [37]. This photo-ionisation cross-section $\sigma_{q\to E_{kin}}^{ion}$ can be related to the free-bound recombination cross-section $\sigma_{E_{kin}\to q}^{rec}$ using Milne's relation [38]. In the previous expression, α is the fine-structure constant, a_0 is the Bohr radius, E_R is the ionisation energy and $G_{nq}^{bf}(\lambda)$ is the so-called bound-free Gaunt factor which acts as a quantum correction for the classically derived cross-section and which usually is close to unity [39, 40].

Combining equations 2.28 - 2.31, while using equation 2.27 to rewrite v in terms of λ and E_q as well as to substitute $dv = \frac{hc}{mv\lambda^2} d\lambda$, results in an expression for the free-bound spectral

emission coefficient [29]:

$$\varepsilon_\lambda^{fb}(\lambda) = \frac{64\sqrt{\pi}c(\alpha a_0)^3 E_R}{3\sqrt{3}}\, n_Z n_e Z^4 \Big(\frac{E_R}{k_b T_e}\Big)^{3/2} \frac{1}{\lambda^2}\, \exp\Big(-\frac{hc}{\lambda k_b T_e}\Big) \times \sum_{n_q > n_{q,min}} \frac{1}{n_q^3}\, \exp\Big(\frac{E_\infty - E_q}{k_b T_e}\Big) G_{nq}^{bf}(\lambda) \quad (2.32)$$

in which $E_\infty - E_q = (Z^2 Er)/n_q^2$ and in which the sum over n_q again adds the contributions of the different bound states.

2.4.2 Bremsstrahlung

In addition to the previously discussed recombination radiation, (free-free) Bremsstrahlung makes up the continuum spectrum. As a result of Coulomb interactions, free electrons are continuously deflected by the electric fields of neighbouring ions. During such a deflection, the electron loses some kinetic energy which is emitted as light. The emission coefficient of free-free transitions can be obtained by replacing the sum over the different excited states in equation 2.32 by an integral over free states [41]:

$$\int_{n_{q,lim}}^{\infty} \frac{1}{n_q^3}\, \exp\Big(\frac{Z^2 Er}{k_b T_e n_q^2}\Big) \mathrm{d}n_q = -\frac{k_b T_e}{2Z^2 Er}\Big[\, \exp\Big(\frac{Z^2 Er}{k_b T_e n_q^2}\Big)\Big]_{n_{q,lim}}^{\infty} \quad (2.33)$$

in which $n_{q,lim}$ is the ionisation limit.

Rewriting the exponent back in terms of $E_\infty - E_q$, makes the integral easier to evaluate, because $E_\infty - E_q = 0$ at the ionisation limit $n_q = n_{q,lim}$ and $E_\infty - E_q = -\infty$ at $n_q \to \infty$. The integral now becomes:

$$-\frac{k_b T_e}{2Z^2 Er}\Big[\, \exp\Big(\frac{E_\infty - E_q}{k_b T_e}\Big)\Big]_{n_{q,lim}}^{\infty} = \frac{k_b T_e}{2Z^2 Er} \quad (2.34)$$

This leads to the following expression for the free-free spectral emission coefficient:

$$\varepsilon_\lambda^{ff}(\lambda) = \frac{32\sqrt{\pi}c(\alpha a_0)^3 E_R}{3\sqrt{3}} n_Z n_e Z^2 \Big(\frac{E_R}{k_b T_e}\Big)^{1/2} \frac{1}{\lambda^2}\, \exp\Big(-\frac{hc}{\lambda k_b T_e}\Big) G^{ff}(T_e, \lambda) \quad (2.35)$$

in which $G^{ff}(T_e, \lambda)$ is the free-free Gaunt factor which again acts as a quantum correction for the classically derived cross-section [39, 40]. In contrast to the free-bound Gaunt factor, the free-free Gaunt factor does not necessarily have to be close to unity.

By adding the free-bound (equation 2.32) and free-free (equation 2.35) components, the total continuum radiation spectrum can be calculated. Figure 2.2a shows such a continuum spectrum for a plasma with $T_e = 5$ eV and $n_e = 10^{20}$ m^{-3}. By looking at the influence of the plasma parameters on the continuum radiation spectrum in the visible part of the spectrum (see figure 2.2b), it can be concluded that n_e mainly determines the total intensity of the emitted light, whereas T_e mainly influences the step-like behaviour caused by recombination.

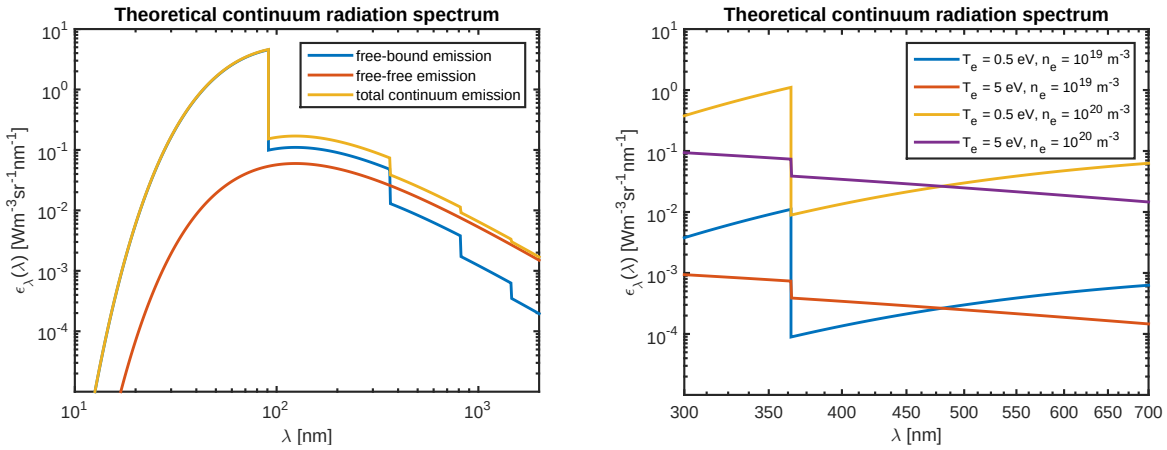

(a) Continuum for $T_e = 5$ eV, $n_e = 10^{20}$ m^{-3}. (b) Continuum for different plasma conditions.

Figure 2.2: Theoretical calculations of the free-bound and free-free components of the continuum radiation spectrum for different divertor-relevant plasma conditions.

2.5 Plasma equilibrium

For the interpretation of the measured radiation, it is common to describe the emitting plasma as either being in a state of (local) thermodynamic equilibrium (TE) or in a non-equilibrium state in which certain processes in the plasma dominate the others.

Thermodynamic equilibrium is defined as a state in which each plasma process is in balance with its reversed process, i.e. both processes have the same reaction rate and cancel each other out, which implies that a plasma in TE satisfies the following balance criteria [42]:

- **The Planck balance** which describes a situation in which absorption of photons by matter is in balance with the (spontaneous and stimulated) emission of photons by matter. When this is the case, the spectral radiance of the system is described by Planck's radiation law.
- **The Maxwell balance** which describes a situation in which the exchange of kinetic energy during inelastic collisions does not lead to a significant heating or cooling of any of the different plasma species. When this balance criterion is satisfied, a Maxwell-Boltzmann distribution can be used to describe the energy distribution of the different species (see equation 2.30 for the corresponding velocity distribution), each characterised by the same temperature.
- **The Boltzmann balance** which holds when the production rate of bound electrons with an energy E_p is in balance with its destruction rate, for each energy level p. In this context, the production of particles in state p is either governed by the de-excitation of particles from a higher energy level or by the excitation of particles from a lower energy level. Similarly, particles are lost due to either excitation to higher energy levels or de-excitation to lower levels. In such a balanced situation, the excited states are populated according to the Boltzmann distribution (in which $q < p$):

$$\frac{n_p}{n_q} = \frac{g_p}{g_q} \exp\Big[- \frac{E_p - E_q}{k_b T} \Big] \tag{2.36}$$

- **The Saha balance** which describes a plasma in which ionisation and recombination are balanced, resulting in a situation in which the distribution of particles over the different ionic states does not change and in which the corresponding distribution function is given by the Saha equation:

$$\frac{n_g^{z+1} n_e}{n_q^z} = 2\frac{g_g^{z+1}}{g_q^z}\Big(\frac{m_e k_b T}{2\pi\hbar^2}\Big)^{3/2} \exp\Big[-\frac{E_\infty - E_q}{k_b T}\Big] \tag{2.37}$$

  in which E_∞ again is the ionisation energy, n_g^{z+1} and n_q^z denote the population density of the different ionisation states with the corresponding statistical weights g_g^{z+1} and g_q^z. If $z = 0$, then n_g^{z+1} denotes a singly ionised ion and n_q^z denotes a neutral atom in an excited state q.

Having described the key balancing criteria that determine whether a plasma is in thermodynamic equilibrium, it must be said that these are only simultaneously satisfied in the core of stars. When radiation escapes from the plasma, for instance, the Planck balance does not hold anymore, leading to a departure from TE. However, when the loss of radiative energy is relatively small compared to the energy exchange between the plasma particles, which is often the case in collision dominated plasmas, the plasma is said to be in local thermodynamic equilibrium (LTE), because the other balances are still satisfied on a local scale. In general, however, fairly large electron densities are required for the plasma to be in LTE, i.e. for a 0.5 eV hydrogen plasma the electron density needs to exceed a value of 10^{23} m^{-3} and for higher temperatures, the minimum density becomes larger as well [21]. As can be seen in figure 1.10, these densities have never been reached in Magnum-PSI before and, therefore, the plasma cannot be considered to be in LTE.

At lower electron densities, collisions become less frequent, effectively limiting the amount of energy transfer between the different plasma species. When this is the case, the electron-ion Maxwell balance criterion is not satisfied and, as such, the plasma species cannot be described by a single temperature anymore (even though the energy distribution of the individual species may still be described by a Maxwell-Boltzmann distribution). At the same time, the excitation of a bound electron between widely separated energy levels becomes less likely at smaller collision frequencies than is the case for closely separated, higher energy levels, causing a violation of the Boltzmann balance. Additionally, transport of particles towards or away from the active plasma region may disturb the Saha balance, resulting in a situation in which either ionisation or recombination is the dominant process. In both these situations, the unfulfilled balance criteria lead to an excited state distribution in which the lower excited states are not in equilibrium anymore, while the closely separated, upper energy levels still are. Such a plasma is said to be in partial local thermodynamic equilibrium (pLTE).

A common way to investigate the deviation from LTE of the excited state population distribution is to plot $\ln(n_p/g_p)$ as function of the energy difference $E_p - E_g$ in a Boltzmann-plot. According to equation 2.36, the population distribution in these Boltzmann-plots should behave linearly with a slope of $-1/k_b T_e$, presuming that the plasma is in equilibrium. However, the lower excited states are often not in equilibrium, as mentioned before, and, as such, these states can either be underpopulated or overpopulated with respect to the linear Boltzmann distribution (see paragraph 4.3). In ionising plasmas, for example, charged particles are

transported away from the plasma, effectively reducing the amount of recombination reactions taking place. Since the ionisation of highly excited states is easiest, i.e. their energy is closest to the ionisation limit, they are removed from the plasma. The consequent drop in the local density is compensated by an inflow of ground-state neutrals. Excitation of these neutrals, predominantly to the lower energy levels, leads to an overpopulation of these states. Conversely, when charged particles diffuse inwards and three-body recombination is dominant, the lower excited states will be underpopulated with respect to pLTE, because three-body recombination acts as a source for higher excited states (see table 1.1). This effect may partially be counteracted by radiative recombination, which mainly populates the lower excited states. However, for divertor-relevant plasma conditions, three-body recombination is still the dominating process ($\approx 90\%$ in the temperature range 0.8 - 1.5 eV) and, as such, it is expected to measure the underpopulation of the lower excited states in the recombining regime [43].

2.6 Collisional-radiative modelling

Even though (p)LTE assumptions cannot be used in non-equilibrium plasmas, it is still possible to determine the excited state population distribution by modelling the formation, excitation and de-excitation of excited hydrogen atoms due to a number of different collisional-radiative (CR) processes. Yacora, which is such a CR-model for hydrogen, does so by evaluating the cross-sections of the collisional-radiative processes that occur between several atomic and molecular hydrogen species. The processes that are taken into account are listed in table 2.2 [22, 23].

Table 2.2: Overview of the collisional processes that determine the population densities of the excited states, which are taken into account in the Yacora CR-model. In this table, energy level p denotes an excited state, whereas q is a lower energetic state.

Description	Reaction	Pop. Coeff.
Atomic Processes		
Excitation by e^-	$H(q) + e^- \rightarrow H(p) + e^-$	R_{0p}
De-excitation by e^-	$H(p) + e^- \rightarrow H(q) + e^-$	R_{0p}
Spontaneous emission	$H(p) \rightarrow H(q) + h\nu$	R_{0p}
Ionization	$H(q) + e^- \rightarrow H^+ + e^- + e^-$	R_{0p}
Three-body recombination	$H^+ + e^- + e^- \rightarrow H(p) + e^-$	R_{1p}
Radiative recombination of H^+	$H^+ + e^- \rightarrow H(p) + h\nu$	R_{1p}
Atomic mutual neutralisation	$H^+ + H^- \rightarrow H(p) + H$	R_{5p}
Molecular Processes		
Dissociation of H_2	$H_2 + e^- \rightarrow H(p) + H(1) + e^-$	R_{2p}
Dissociation of H_2^+	$H_2^+ + e^- \rightarrow H(p) + H^+ + e^-$	R_{3p}
Dissociative recombination of H_2^+	$H_2^+ + e^- \rightarrow H(p) + H(1)$	R_{3p}
Dissociative recombination of H_3^+	$H_3^+ + e^- \rightarrow H(p) + H_2$	R_{4p}
Molecular mutual neutralisation	$H_2^+ + H^- \rightarrow H(p) + H_2$	R_{5p}

Each of these processes affects the population density of a certain excited state n_q of the hydrogen atom. For atomic processes only, the temporal dependence of the population density can be described by the following rate equation:

$$\frac{\mathrm{d}n_q}{\mathrm{d}t} = \sum_{p>q} A_{pq} n_p - \sum_{p<q} A_{qp} n_q + n_e \left(\sum_{p \neq q} X_{pq} n_p - \sum_{p \neq q} X_{qp} n_q + (\alpha + \beta n_e) n_+ - S_q n_q \right) \quad (2.38)$$

in which A_{pq} and A_{qp} represent the transition probabilities for spontaneous emission, X_{pq} and X_{qp} are the rate coefficients for excitation and de-excitation by electron-impact, α and β are the rate coefficients for radiative recombination and three-body recombination and S_q is the rate coefficient for ionization. Beware that the molecular processes of table 2.2 are not taken into account in equation 2.38. However, the given expression can be extended with several other terms, consisting of a rate coefficient multiplied by the particle densities of the involved species, to include these processes. The rate coefficients in this equation all depend on the electron density n_e and temperature T_e.

Instead of looking at the individual processes, CR-models often group the different processes based on the involved plasma species. In that case, so-called population coefficients R_{sq} are used to quantify the coupling between the different plasma species and the excited states. Table 2.2 shows for each process to which population coefficient it contributes. These coefficients are defined by the following expression:

$$R_{sq} = \frac{n_q}{n_e n_s} \quad (2.39)$$

in which s denotes the different plasma species ($s = 0, 1, 2, 3, 4, 5$ respectively represents H, H^+, H_2, H_2^+, H_3^+, H^-), while q indicates the excited state that is being considered, e.g. R_{24} quantifies the amount of excitations to the fourth energy level, as a consequence of the presence of H_2.

In general, the population density of an excited state in equilibrium can be related to the quasi-constant ground state densities of the different plasma species, by the following equation:

$$n_q = R_{0q} n_e n_H + R_{1q} n_e n_{H^+} + R_{2q} n_e n_{H_2} + R_{3q} n_e n_{H_2^+} + R_{4q} n_e n_{H_3^+} + R_{5q} n_e n_{H^-} \quad (2.40)$$

After solving this equation for a specific energy level, the acquired population density n_q can be used with equation 2.3 to predict the line emission corresponding to the transitions $q \to p$ for $p < q$.

2.7 Summary

If the plasma parameters (T_e and n_e) and the ground-state densities of the different plasma species (n_H, n_{H^+}, n_{H_2}, $n_{H_2^+}$, $n_{H_3^+}$ and n_{H^-}) can be determined reliably, equation 2.40 can be used to calculate the excited state densities n_q. By checking whether the calculated values of n_q correspond to the measured excited state densities, it is possible to validate the Yacora

CR-model. However, as mentioned in paragraph 1.8, the actual validation will not be carried out during this project, since the ground-state densities of the plasma species are unknown, while this project mainly deals with experimentally determining n_q.

Equation 2.3 can be used to obtain the population of any excited states n_q from the emission coefficient ε_{qp} corresponding to the radiative transition $q \to p$. In the specific case of the Balmer lines (see table 2.1), which can easily be measured, the transition $q \to 2$ is used. A spectrometer, however, measures the spectral radiance L_λ that is emitted by the plasma, as given by equation 2.5. By using multiple lines-of-sight through the plasma, an Abel inversion (see paragraph 3.5) can be used to obtain spectral emission coefficients ε_λ^{qp}. In order to get the desired emission coefficients corresponding to a certain Balmer line, spectral line broadening should be taken into account, as indicated by equation 2.4. Therefore, the different broadening mechanisms have been discussed in paragraph 2.3. The spectrum also contains continuum radiation (see paragraph 2.4), which is present in the background and should be subtracted from the integrated signal to obtain the actual emission coefficients.

Chapter 3

Set-up and data analysis

This chapter explains how to obtain the excited state density profiles from the raw data using the multi-chord spectrometer set-up. In order to do so, the set-up and its main properties will be discussed. Additionally, this chapter deals with the necessary intensity and wavelength calibrations and the spectral fitting and Abel inversion procedures that are required to determine local emission coefficients.

3.1 Multi-chord spectrometer set-up

In order to answer the research question as posed in paragraph 1.8, a multi-chord spectrometer set-up has been realised and installed on Magnum-PSI. This paragraph describes the set-up focusing on the following three parts: the spectrometer, the viewing system and the camera.

3.1.1 The Jarrell-Ash spectrometer

The core of the set-up is formed by an old Jarrell-Ash 78-466 spectrometer, which is of Czerny-Turner design (see figure 3.1). Light enters the system via a fiber array that is positioned in front of the entrance slit of the spectrometer (more about the fiber array in paragraph 3.1.2). The original curved entrance slit was replaced by a straight slit to enable the use of all 40 optical fibers of the array. A concave collimating mirror ($f = 1.0$ m) reflects the incoming light towards a replaceable plane grating inside the spectrometer, which separates the light into its constituent colours. For that purpose, the diffraction grating relies on a combination of constructive and destructive interference, which results in a pattern of maxima and minima in the intensity of the reflected light. For a given wavelength, the mth order intensity maximum gets reflected at an angle θ_m:

$$\sin(\theta_i) + \sin(\theta_m) = \frac{m\lambda}{d} \tag{3.1}$$

in which θ_i is the angle of incidence of the collimated light beam and d indicates the spacing between the grooves of the grating. Often d is given in terms of a grating constant $a = 1/d$ which specifies the number of grooves per millimeter.

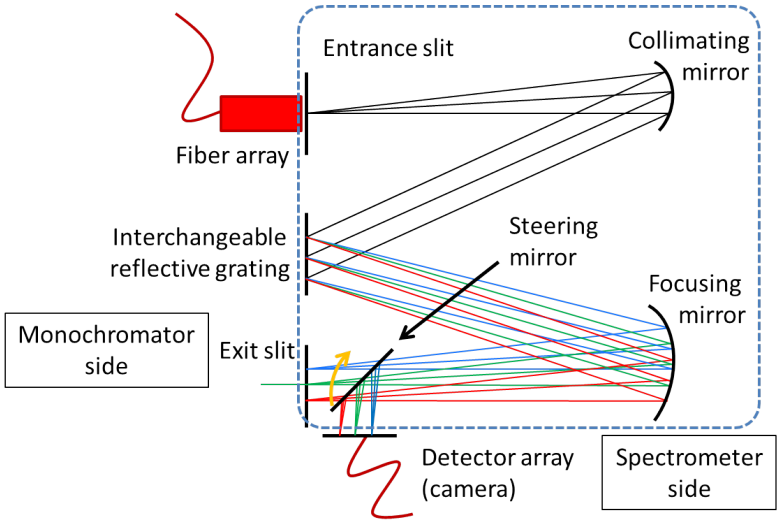

Figure 3.1: A schematic overview of a spectrometer/monochromator in Czerny-Turner geometry. The reflective grating splits the incoming bundle of light into its constituent colours, which each exit the spectrometer at a slightly different location. The steering mirror can be moved in such a way that it either reflects the light towards the spectrometer side of the machine or that it is not in front of the exit slit, allowing the light to exit the machine at the monochromator side.

The concave focussing mirror, which also has a focal length of 1.0 m, makes sure that the collimated light beams are focused onto the camera (for spectrometer-mode) or the exit slit (for monochromator-mode). A steering mirror near the end of the optical path inside the spectrometer can be moved as shown by the orange arrow in figure 3.1 in order to select either mode of operation. The monochromator-mode has not been used during this project, since it is only useful when looking at light of a specific colour, because this exit of the spectrometer is very narrow and, therefore, only allows a small band of colours to pass.

The replaceable diffraction grating is a key feature of this set-up, because the spectral range and spectral resolution of the spectrometer depend on the grating constant of the grating that is being used. A grating with a large number of lines per millimeter, for instance, has a high spectral resolution in a relatively small spectral region, whereas a grating with a small grating constant is capable of observing a relatively large spectral range at a low spectral resolution. The spectral range $\Delta\lambda$ and the spectral resolution $\delta\lambda$ of the set-up are respectively given by the following expressions [44]:

$$\Delta\lambda = L_d P = n_p w_p \frac{d\,\cos(\theta_m)}{mf} \tag{3.2}$$

and

$$\delta\lambda = w_s P = w_s \frac{\Delta\lambda}{n_p w_p} = w_s \frac{d\,\cos(\theta_m)}{mf} \tag{3.3}$$

in which w_s is the width of the entrance slit, L_d is the effective width of the detector, i.e. the number of pixels n_p multiplied by the width of a single pixel w_p, and P is the reciprocal linear dispersion, which indicates the spectral range covered in a certain distance and which can be expressed in terms of d, m, θ_m and the focal length f of the spectrometer.

Table 3.1: An overview of the properties of the available gratings.

Grating type	a [ln/mm]	$\Delta\lambda$ [nm]	$\delta\lambda$ [nm]	Features of interest
Low resolution	150	185	0.5	Overview spectrum and Balmer lines
High resolution	2400	10	0.015	Fulcher band and peak shapes

Table 3.1 lists the different properties of the two available gratings that were used during this project. The low-resolution grating ($a = 150$ ln/mm) has been used to measure a wide-ranged overview spectrum. In particular, its purpose is to measure the Balmer-spectrum, since its relatively large spectral range enables the spectrometer to observe H-β up to H-θ without having to rotate the grating. Alternatively, the grating can be turned in such a way that it is possible to measure the H-α line, while H-β is observed just at the edge of the detector. The high resolution grating ($a = 2400$ ln/mm) is required to measure the Fulcher band, because of the relatively small spacing between the different ro-vibrational molecular lines.

3.1.2 The viewing system

The purpose of the viewing system is to capture the light that is emitted by the plasma and to relay it to the multi-chord spectrometer in an adjacent room. Figure 3.2 shows a schematic overview of the viewing system that has been placed 5.0 cm in front of the windows looking at the same position as the Thomson scattering system at an angle of 45° upward into the target chamber of Magnum-PSI. An achromatic doublet lens ($f = 10$ cm) is used to image

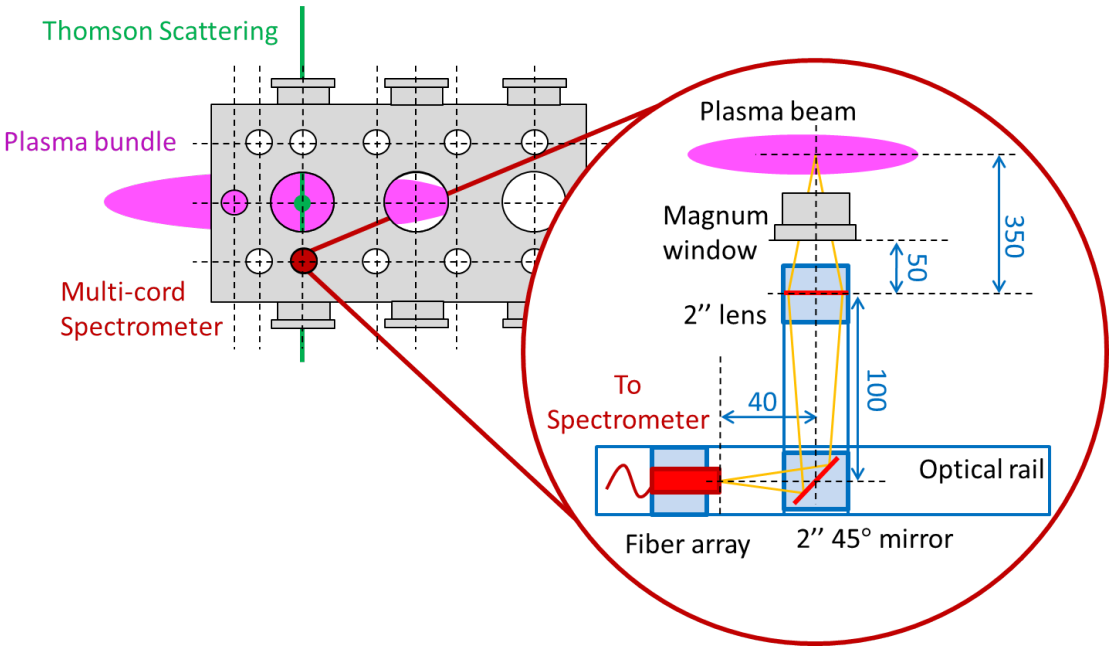

Figure 3.2: A schematic overview of the viewing system that is being used for the multi-chord spectrometer, showing its components and geometrical configuration as well as its position with respect to the target chamber of Magnum-PSI. Lengths are given in mm.

the plasma via a 45° broadband dielectric mirror onto the head of a Ceramoptec fiber array. This fiber array contains 40 fused silica optical fibers with a diameter of $d = 0.4$ mm and a numerical aperture of $NA = 0.22$.

The geometry of the viewing system is such that it manages a magnification factor of $M = 0.4$ and observes a plasma beam with a diameter of 4.5 cm. The viewing system is designed so that it can easily be modified to increase the observed beam diameter up to 5.4 cm with a corresponding magnification factor of $M = 0.33$. In order to do so, the focusing lens should be moved 5.0 cm backwards (object distance becomes $x_1 = 40$ cm to the core of the plasma), while the fiber head should be retracted 4.3 cm (resulting in an image distance of $x_2 = 13.3$ cm from the lens). In the current design, the mirror cannot be moved and, therefore, keeps its original position.

3.1.3 The Pixis camera system

The multi-chord spectrometer has been equipped with a Princeton Instruments PIXIS 2048B camera [45]. The system uses a CCD array with a good quantum efficiency in the visible part of the spectrum (as shown in figure 3.3) that has 2048×2048 pixels of 13.5×13.5 μm. The camera is cooled to -55°C to reduce the dark current to a typical value of 0.005 electrons per pixel per second. The camera uses a 16-bit A/D converter and the readout noise is typically in the order of 12 electrons at a conversion speed of 2MHz, resulting in a dynamic range of 8333. Unfortunately, the camera has a relatively slow shutter and readout speed ($t_r \approx 2.3$ s), making the set-up unsuitable for real-time imaging in rapidly changing plasmas. However, since the set-up is mainly used for steady-state plasma operation instead, a long exposure time and the possibility of averaging over multiple frames improves the signal-to-noise ratio and reduces the influence of fluctuations inside the plasma on the measured signal.

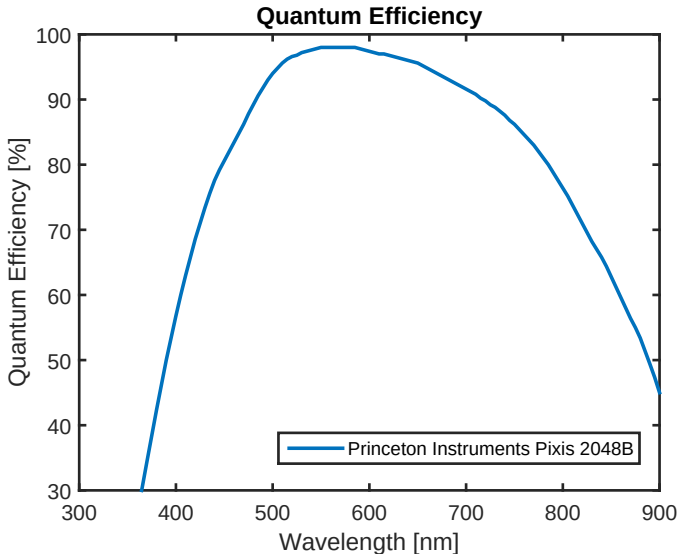

Figure 3.3: The quantum efficiency of the Princeton Instruments PIXIS 2048B camera as function of the wavelength [45].

3.1.4 Key characteristics of the set-up

In the previous paragraphs, the multi-chord spectrometer set-up that has recently been installed on Magnum-PSI, has been described. In this section, this new system will be compared to the Avantes spectrometer, which is a well-established diagnostic on Magnum-PSI. First, however, the main features of interest of the new multi-chord spectrometer will be summarised once more:

- **Multi-chord spectroscopy** is facilitated by the use of a fiber array consisting of 40 fibers, each looking with a different line of sight through the plasma beam. By combining the measurements of multiple fibers using an Abel inversion (see paragraph 3.5), local emissivities can be obtained with a spatial resolution Δr of 1.1 mm at a magnification of $M = 0.33$ or 1.4 mm at $M = 0.4$.
- **The interchangeable grating** makes it possible to use the multi-chord spectrometer as an overview spectrometer (using a grating with a low grating constant a) or as a high-resolution spectrometer (using a high a grating).
- **The rotatable grating mount** enables the spectrometer system to scan along the wavelength axis, making it possible look at different parts of the spectrum. The quantum efficiency of the camera (see figure 3.3), however, only allows the system to look at the visible part of the spectrum; ultraviolet or infra-red light cannot be observed properly with the current camera system.
- **An intensity calibration** has been carried out using a Labsphere calibration lamp to convert camera counts into absolute radiances (see paragraph 3.2.2). This is a crucial step when determining absolute excited state densities.
- **The longitudinal viewing location** corresponds to the location at which Thomson scattering measurements are available. This is noteworthy, because the Thomson scattering system provides radial T_e and n_e profiles of the same plasma that emits the light that is being measured by the multi-chord spectrometer [27]. In principle, however, the longitudinal position can be changed, making it possible to observe the upstream plasma, but then T_e and n_e will be unknown.

The Avantes spectrometer, which is readily available on Magnum-PSI, is not as flexible as the multi-chord spectrometer, since it uses 6 fixed channels to observe different parts of the spectrum at fixed resolutions. Moreover, due to the limited access for diagnostics on Magnum-PSI, different channels have different lines of sight through the plasma and, as such, it is only possible to have three channels look in a radial direction through the plasma at the same position of the Thomson scattering system. Finally, and most importantly, each channel uses a single fiber, which makes it impossible to do spatially resolved measurements with the Avantes spectrometer.

Even though the channels of the Avantes are fixed, the system covers almost the entire visible part of the spectrum at once, whereas the multi-chord spectrometer can only cover 185 nm (see table 3.1) at the same time. Furthermore, the Avantes system is much faster, making it more suitable for monitoring the emission of the plasma during a shot. Finally, the Avantes is more reliable in terms of repeatability, since rotating the grating of the multi-chord spectrometer is controlled manually and affected by hysteresis and, maybe more importantly, the positioning of the grating inside its mount is not reproducible when switching gratings.

3.2 Data acquisition

3.2.1 Obtaining spectra

The PIXIS camera is operated by the LightField-software, which also takes care of the data acquisition. In order to accumulate as much signal as possible, the exposure time of the camera is preferably set to be as long as possible without over-saturating the CCD array. Additionally, the software averages multiple exposures per frame to reduce shot noise and the effect of plasma fluctuations and to improve the signal-to-noise ratio. A background image, taken with the exact same settings in the absence of a plasma, is subtracted from the original image to reduce the influences of stray light, dark current and readout noise.

In order to correct for a small rotational miss-alignment of the fiber array with respect to the CCD array of the camera, the image is slightly rotated (typically $\approx 0.5°$) after background subtraction, to make sure that each fiber is projected horizontally. The image shown in figure 3.4a, however, has not been rotated and, as such, the red and purple horizontal lines do not divide the different fibers correctly, which is especially visible for H-ϵ to H-θ. For the actual analysis (and also for image 3.4b) the required rotational correction has been applied and will not be mentioned again. The positions of the red and puple horizontal lines are based on a vertical cross-section of the rotated camera image, as shown in figure 3.4b for the Balmer H-β line. Each of the 40 fibers is clearly distinguishable as a single peak and it is also clearly visible at which pixels the edges of each fiber are located. After having identified which horizontal pixel rows belong to a certain fiber, the total signal for each fiber is obtained by vertically binning these rows (the rows between the horizontal lines in figure 3.4a). This results in 40 spectra similar to the one shown in figure 3.5a, each taken for a different line-of-sight through the plasma. Finally, figure 3.4b clearly shows that the transmission of each fiber can be different (especially fiber 15 has a reduced transmission), possibly due to

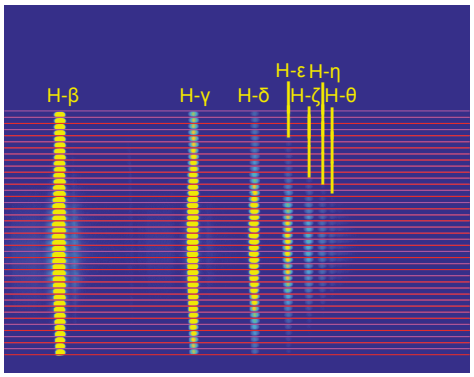

(a) Multi-chord camera image with spectral lines.

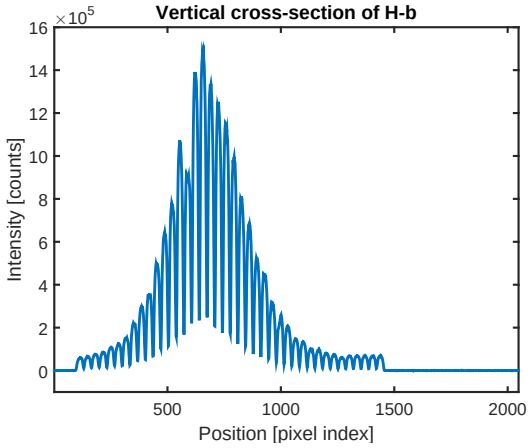

(b) Vertical cross-section of the H-β line.

Figure 3.4: These figures illustrate how the different fibers are being located based on the raw images as taken by the PIXIS camera system.

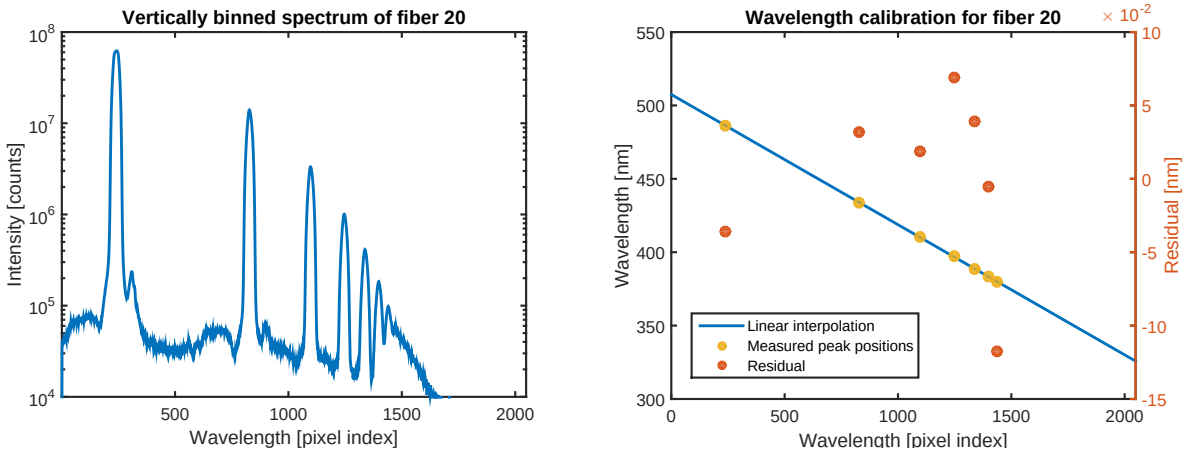

(a) Single fiber spectrum.

(b) Wavelength calibration.

Figure 3.5: The uncalibrated Balmer-spectra of each fiber is used to define a wavelength axis based on the positions of identified lines. The spectral peaks shown in figure (a) correspond to transitions from H-β up to H-θ.

the fiber being slightly damaged. This effect, however, will be corrected by the intensity calibration that will be discussed in the next paragraph.

For each fiber spectrum, the corresponding wavelength axis is defined using a linear interpolation based on the wavelengths corresponding to known spectral peaks in the measured spectrum or in a different spectrum that has been obtained using the exact same spectrometer settings. The linear interpolation method gives wavelength values accurate up to approximately 0.15 nm, as can be seen based on the residuals in figure 3.5b. Since this accuracy is comparable to the width of the spectral peaks (see paragraph 3.4), it is deemed unnecessary to use polynomials of a higher degree for the wavelength calibration. Unfortunately, it is not possible to develop a standard wavelength calibration procedure that defines a wavelength axis based on the wavelength that is displayed on the spectrometer itself. This is because hysteresis in the mechanical rotation system of the spectrometer makes it impossible to reliably reproduce the same grating position at a given displayed wavelength.

3.2.2 Absolute intensity calibration

After the wavelength calibration, an intensity calibration has been carried out to convert camera counts into actual radiometric quantities and to enable a direct comparison between the different fibers. In order to do this calibration, the spectrum of a source with a known spectral radiance (in $\mathrm{Wm^{-2}sr^{-1}nm^{-1}}$) is measured, following the procedure as described in paragraph 3.2.1, while using the exact same set-up as has been used to measure the uncalibrated spectra. During this project, a Labsphere integrating sphere has been used for this purpose, which relies on a tungsten halogen light source with a known spectral radiance (see figure 3.6b) [46]. The integrating sphere, also known as an Ulbricht sphere, uses a reflective spherical cavity with a diffusive coating on the inside to make sure that the light emitted by the light source exits the sphere uniformly. It must be noted that the spectral radiance of the Labsphere has been measured last in 2007, which could mean that

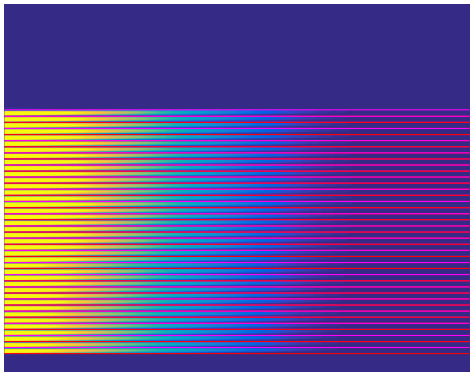

(a) The Labsphere spectrum as measured by the PIXIS-camera.

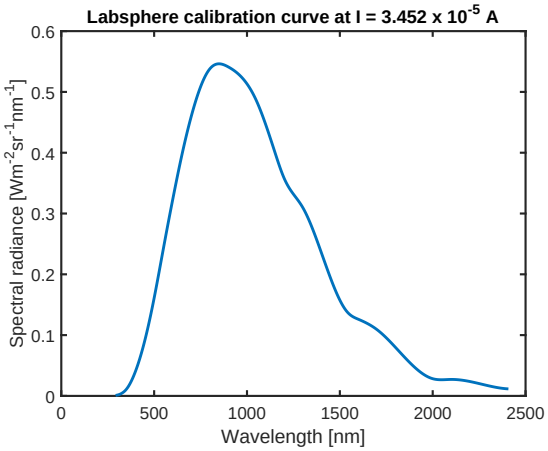

(b) Expected Labsphere radiance [46].

Figure 3.6: The intensity calibration has been carried out using a Labsphere and a tungsten halogen lamp with a known spectral radiance.

the reference spectrum in figure 3.6b is out-dated, because the emission of the lamp and the transmission of the reflective coating deteriorate over time.

Using a Labsphere calibration measurement, a signal S (in counts) can be converted into a spectral radiance $L_S(\lambda)$ using the following expression, which is valid as long as the optics of the viewing system are fully filled by the light source:

$$L_S(\lambda) = \frac{I_{sp}}{I_{cal}} \frac{S}{S_{sp}} L_{cal}(\lambda) \tag{3.4}$$

in which $L_{cal}(\lambda)$ is the radiance of the calibrated light source as given in 3.6b, S_{sp} is the measured signal (in counts) as measured during the Labsphere intensity calibration measurement, I_{sp} is the measured current through the light source during the Labsphere calibration and I_{cal} is the current through the light source during the measurement of the calibration curve ($I_{cal} = 3.452 \cdot 10^{-5}$ A).

By considering the geometry of the spectrometer, it is possible to determine the solid angle of the light that is being captured by a single fiber as well as the area of the surface that emits the light. Together with equation 2.5, these quantities can be used to obtain an absolute intensity calibration in terms of a spectral flux Φ_λ (in W/nm) or a spectral photon flux, i.e. the number of photons emitted at a given wavelength during a certain period of time.

As previously discussed in paragraph 3.1.2, the set-up has a magnification factor of $M = 0.4$ and the diameter of the optical fibers is $d_f = 0.4$ mm. This means that the observed area of a single fiber equals $\pi(r_f/M)^2 = 0.8$ mm^2. When determining the solid angle, it is important to consider which component of the set-up has the smallest acceptance angle. As shown in figure 3.7, the grating turns out to be the limiting component, since it only accepts light that exits the optical fiber at an maximum angle of $\theta_{gr} \approx 6.0°$. The corresponding observation angle is then $\theta_{ob} \approx 2.4°$, which results in an observed solid angle of $\Omega = 2\pi(1 - \cos(\theta_{ob})) \approx 5.5 \cdot 10^{-3}$ sr.

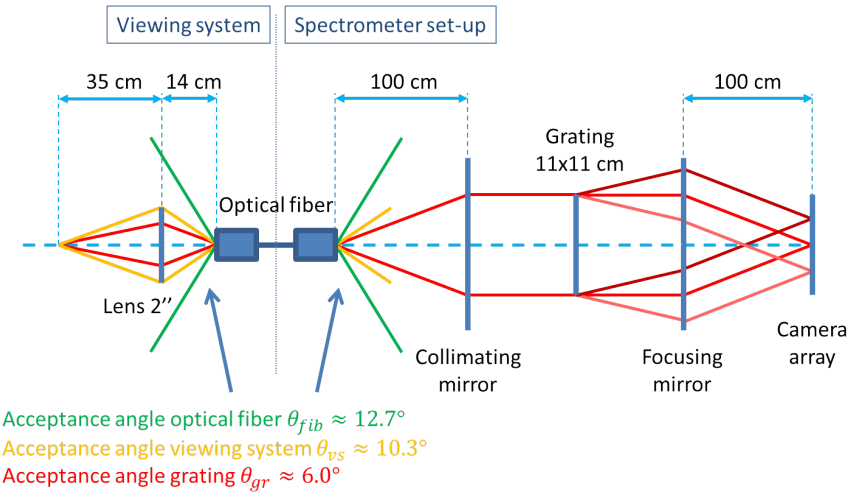

Figure 3.7: A schematic overview of the angles involved with the optical set-up. The green angle indicates the acceptance angle of the optical fiber, the orange angle indicates the angle at which the light from viewing system entrances the optical fiber and the red angle shows the light that reaches the grating.

3.3 Instrumental line broadening

As mentioned in paragraph 2.3.1, imperfections in the optical set-up and a finite-sized opening of the entrance slit are partially responsible for the broadening of spectral lines. In order to quantify this broadening effect, the instrument function of the spectrometer has been determined by measuring the FWHM of a spectral line from a low-pressure discharge tube. When using such a tube, the effects of other broadening mechanisms can be neglected due to the low temperatures and pressures inside the lamp, making instrumental broadening the primary cause of spectral broadening. Figure 3.8 shows the FWHM of the H-γ line as function of the width of the entrance slit of the spectrometer. The choice for H-γ as spectral

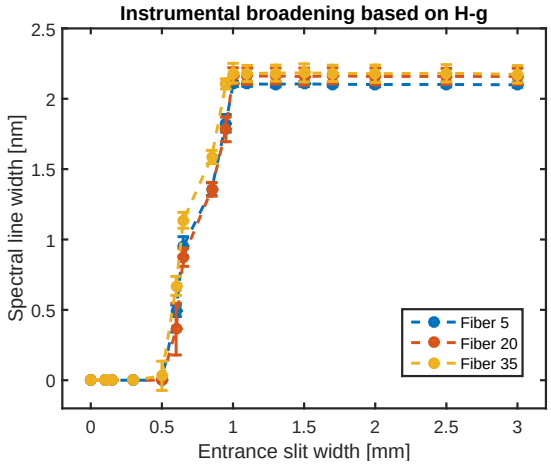

Figure 3.8: Instrumental broadening of H-γ as function of the slit width.

Table 3.2: An overview of the line broadening mechanisms and their estimated maximum effect on the line shapes of respectively H-β and H-θ, as calculated by the equations in paragraph 2.3.1.

	$\delta\lambda_\beta$ [nm]	$\delta\lambda_\theta$ [nm]	Parameters for overestimated FWHM
Doppler broadening	$3.7 \cdot 10^{-2}$	$2.9 \cdot 10^{-2}$	$T_a < 1$ eV [47]
Van der Waals broadening	$1.2 \cdot 10^{-4}$	$2.1 \cdot 10^{-3}$	$T_g > 300$ K (room temperature) $0.3 < p_{bg} < 16$ Pa (chapter 4) $\alpha = 4.5\ a_0^3 = 6.67 \cdot 10^{-31}$ m^3 [48, 49] $E_H = E_{IP} = 13.6$ eV, $E_2 = 10.2$ eV, $E_4 = 12.7$ eV, $E_{10} = 13.5$ eV [31]
Resonance broadening	$2.0 \cdot 10^{-5}$	$1.2 \cdot 10^{-5}$	$T_g > 300$ K (room temperature) $0.3 < p_{bg} < 16$ Pa (chapter 4) $\lambda_{R2} = 121.6$ nm, $\lambda_{R4} = 97.3$ nm, $\lambda_{R10} = 92.1$ nm [31] $f_{R2} = 4.16 \cdot 10^{-1}$, $f_{R4} = 2.90 \cdot 10^{-2}$, $f_{R10} = 1.61 \cdot 10^{-3}$ [50]
Stark broadening	$9.5 \cdot 10^{-2}$	$4.6 \cdot 10^{-1}$	$n_z \approx n_e < 2.5 \cdot 10^{20}$ m^{-3} (chapter 4)
Natural broadening	$6.5 \cdot 10^{-6}$	$1.7 \cdot 10^{-6}$	$\tau_2 = 4.7 \cdot 10^{-8}$ s, $\tau_4 = 3.3 \cdot 10^{-8}$ s, $\tau_{10} = 1.9 \cdot 10^{-6}$ s [31]
Instrumental broadening	2.2	2.2	$w_s = 1.5$ mm

line is based on the fact that this line was measured in the middle of the CCD-array and, therefore, has the best wavelength calibration (see figure 3.5b). Other spectral lines show a similar behaviour.

During the experiments, the width of the entrance slit was chosen to be approximately 1.5 mm such that the absolute calibration described in paragraph 3.2.2 holds and such that the slit would not affect the throughput and the signal-to-noise ratio of the different fibers differently. Using figure 3.8, it can be concluded that the instrument in this case accounts for a spectral line broadening of $\delta\lambda \approx 2.2$ nm. As can be seen in table 3.2, this means that instrumental line broadening in the current set-up dominates the other line broadening mechanisms. Because a high spectral resolution was not crucial to the measurements carried out during this project, a wide slit opening could easily be used, as long as the different spectral lines could be resolved from each other (see paragraph 3.4). Nevertheless, it could prove to be useful to make the entrance slit narrower in future experiments, in order to improve the spectral resolution. This, however, requires a better alignment of the fiber array with respect to the entrance slit in order to guarantee that each fiber is affected similarly by a narrow slit width.

3.4 Spectral fitting and total line radiances

After the LabSphere calibration, the measured spectra are given in terms of a spectral radiance $L_S(\lambda)$ as indicated by equation 3.4. In order to obtain the total line radiance L_{qp}

for each spectral transition, the area underneath each spectral peak needs to be determined. A simple numerical integration method is not adequately suitable for this purpose, because it does not take the background of continuum radiation (see paragraph 2.4) into account. Moreover, the overlap between different spectral peaks starts to play an increasingly important role at decreasing λ, due to the decreasing distance between adjacent peaks and their finite widths. Even though subtracting an estimated background from the measured signal is a possibility, a numerical integration method is not a viable solution, since it cannot separate the different spectral lines in case of overlap.

Therefore, a spectral fitting routine [51] has been used to fit the shape of the spectral peaks from H-β up to H-θ for each fiber. The routine has been specifically designed to fit one or multiple Voigt profiles at given positions λ_0 with arbitrary amplitudes A on top of a given background. The fitting routine has two key settings which determine how the fitting procedure is carried out:

- **The number of peaks** that determines how many Voigt profiles the fitting routine uses to approximate the input spectrum. It is important to make sure that the input data is chosen accordingly. For example, when trying to fit the entire spectrum (H-β up to H-θ) at once, the number of peaks should be set to 7. Alternatively, it is possible to fit each peak separately or anything in between.
- **The background type** that controls the behaviour of the background that will be used during the fitting procedure. Amongst the possible background types are: a constant background, a linear background or no background at all.

Because the fitting routine does not work with a single background profile that resembles the continuum as described by equations 2.32 and 2.35, the continuum is locally approximated by a linear background. This approximation breaks down when considering a large part of the spectrum at once, as can be seen in figure 2.2. Consequently, spectral peaks are preferably considered separately. However, starting at the H-ζ line (see figure 3.9b), adjacent peaks start to have a significant overlap and should therefore be considered together.

Having decided on the fit settings, it is important to consider the different fitting parameters. Each of them should be given an initial value as well as an upper and lower bound. The fitting routine uses the following fit parameters:

- **The linear background** which is characterised by its values at either side of the considered part of the spectrum. In the case of well-isolated lines, the background values are chosen in such a way that they correspond to the average value of the measured signal at the edges of the input data within a margin of 2%. When overlap between spectral peaks starts to play a role, the background value at the low-λ side of the spectrum cannot be determined as accurately using the same method, therefore, the bounds are extended to 20% to give the fitting routine more freedom.
- **The position of each peak** which is precisely known and given by the values in table 2.1. The upper and lower bounds are determined by the wavelength calibration as shown in figure 3.5b.
- **The corresponding peak amplitude** which can easily be estimated by finding the maximum value between the upper and lower position bounds.

- **The peak shape** which is indicated by a number between 0 (for a pure Lorentzian peak profile) and 1 (for a pure Gaussian profile). As indicated by table 3.2, the spectral line profiles are almost completely dominated by the instrument function and, as such, the peak shape is expected to be Gaussian: 0.99 ± 0.01.
- **The width of the peak** which is also determined by the instrument function of the spectrometer and, therefore, estimated to be approximately 2.2 ± 0.1 nm, as can be seen in figure 3.8.

Figure 3.9 illustrates the fitting procedure that has been described in this paragraph for either a single spectral line or multiple lines together. As can be seen in figure 3.9a, the wings of the spectrum are sometimes overestimated by the fitting routine. This is possibly caused by the finite slit width, since the convolution of the spectrum with the instrument function makes the spectral line more narrow. This reasoning also explains why the overestimation is more often the case for the first Balmer-lines (H-β up to H-δ), because these lines are more isolated. The result is a line shape which cannot be described by a combination of a Gaussian and Lorentzian profile and, as such, the fitting routine will not be as accurate at the wings of the profile. This, however, does not matter too much, since the difference in area between both curves makes up only 2 % of the total.

Instead of using a Voigt profile (see equation 2.23), the fitting routine uses a Voigt approximation that is equivalent to the pseudo-Voigt profile described by equation 2.24:

$$\phi_V(\lambda, w) = A\frac{(1-\gamma)\phi_L(\lambda, w) + \gamma\phi_G(\lambda, w)}{(1-\gamma)\phi_L(\lambda_0, w) + \gamma\phi_G(\lambda_0, w)} \tag{3.5}$$

in which w instead of f now denotes the FWHM of the Voigt profile. The shape factor is reversed in this equation, meaning that ϕ_V is fully Gaussian when the shape factor γ equals 1, whereas the pseudo-Voigt of equation 2.24 is a Gauss profile when its shape factor η is 0. Similarly, a Lorentzian profile is obtained when respectively $\gamma = 0$ and $\eta = 1$.

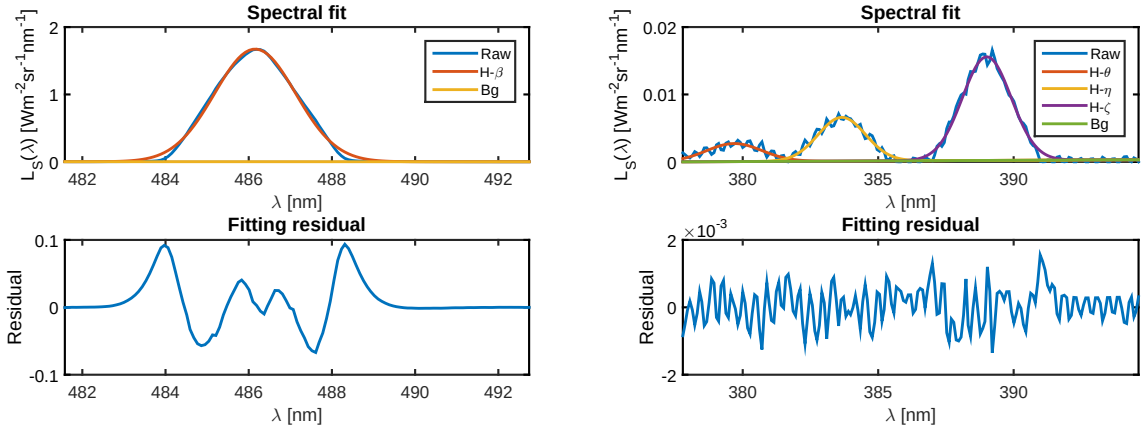

(a) The H-β line.

(b) The H-ζ, H-η and H-θ lines.

Figure 3.9: The spectral fitting procedure applied to a single peak (H-β) and multiple peaks (H-ζ up to H-θ) at once, showing the raw measurement data as well as the estimated peak shapes and linear background. The resulting fitting parameters are shown in table 3.3.

Table 3.3: The obtained fitting parameters as well as the corresponding line radiances for the cases shown in figure 3.9.

	Sym.	H-β	H-ζ	H-η	H-θ
Background (high λ) [$\mathrm{Wm^{-2}sr^{-1}nm^{-1}}$]	bg_r	$2.13 \cdot 10^{-3}$	$3.12 \cdot 10^{-4}$	$3.12 \cdot 10^{-4}$	$3.12 \cdot 10^{-4}$
Background (low λ) [$\mathrm{Wm^{-2}sr^{-1}nm^{-1}}$]	bg_l	$1.22 \cdot 10^{-3}$	$9.85 \cdot 10^{-5}$	$9.85 \cdot 10^{-5}$	$9.85 \cdot 10^{-5}$
Peak position [nm]	λ_0	486.15	389.01	383.66	379.68
Peak height [$\mathrm{Wm^{-2}sr^{-1}nm^{-1}}$]	A	1.67	$1.54 \cdot 10^{-2}$	$6.49 \cdot 10^{-3}$	$2.68 \cdot 10^{-3}$
Peak shape	γ	1.00	1.00	1.00	0.99
Peak width [nm]	w	2.29	2.12	2.06	2.41
Line radiance [$\mathrm{Wm^{-2}sr^{-1}}$]	L_{qp}	4.07	$3.48 \cdot 10^{-2}$	$1.42 \cdot 10^{-2}$	$6.90 \cdot 10^{-3}$

Relating the newly defined shape factor γ to the old one η is easily done by using $\gamma = 1 - \eta$. The main difference between both profiles is that the amplitude of the Voigt profile given by equation 3.5 can have any arbitrary value, instead of being completely dictated by the required normalisation of the area underneath the curve of the pseudo-Voigt. As such, the amplitude of the Voigt function used by the spectral fitting routine is determined by normalising the amplitude of the profile given by equation 2.24 and multiplying this by the actual measured amplitude A.

The total line radiance L_{qp} for each spectral transition can now be obtained by using the obtained fitting parameters to calculate the area underneath the fitted curve with the following expression:

$$L_{qp} = \int_{-\infty}^{\infty} \phi_V(\lambda, w)\mathrm{d}\lambda = \frac{1}{2}A\Big[\eta\frac{\mathrm{sqrt}(\log(2)/\pi)}{|w|} + (1-\eta)\frac{1}{\pi|w|}\Big]^{-1} \tag{3.6}$$

For the examples shown in figure 3.9, the obtained fitting parameters as well as the corresponding line radiances are tabulated in table 3.3.

3.5 Abel inversion and radial emission profiles

3.5.1 The concept of Abel inversions

Because each fiber of the multi-chord spectrometer simultaneously observes the emission of the plasma beam at a different distance y from the horizontal plane going through the centre of the plasma, it is possible to obtain line-of-sight (LOS) profiles of the total line radiance $L_{qp}(y)$ for each spectral transition as function of y. Assuming that the plasma is optically thin, each fiber observes the radiation emitted by the plasma along its corresponding line-of-sight, meaning that the measured line radiances are integrated along the entire LOS.

Assuming that the plasma beam is cylindrically symmetric, the integrated LOS-profiles are related to the radial emission coefficients profiles $\varepsilon_{qp}(r)$ by the following expression:

$$L_{qp}(y) = 2\int_0^{x_m} \varepsilon_{qp}(r)\ \mathrm{d}x = 2\int_0^{\sqrt{R^2-y^2}} \varepsilon_{qp}(r)\ \mathrm{d}x = 2\int_y^R \frac{\varepsilon_{qp}(r)r}{\sqrt{r^2-y^2}}\ \mathrm{d}r \tag{3.7}$$

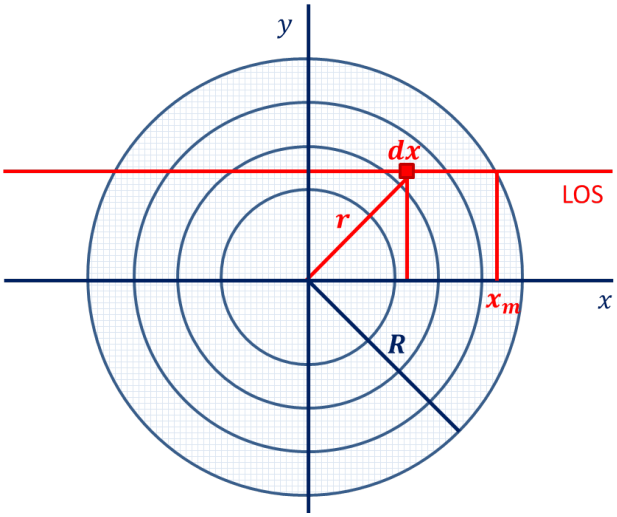

Figure 3.10: A schematic overview illustrating the geometry that is used to relate LOS and radial profiles to each other via an Abel transform.

This equation, often referred to as an Abel transform, is essentially the same as equation 2.5, but modified for the cylindrical geometry as shown in figure 3.10.

A reversed Abel transform, or Abel inversion [52], makes it possible to retrieve local plasma emission coefficient profiles $\varepsilon_{qp}(r)$ by combing line integrated measurements of adjacent lines-of-sight. Starting with the outermost fiber of which the LOS only goes through the edge of the plasma, measures the local emission $\varepsilon_{qp}(R)$ at a radial position R. Each subsequent fiber measures the accumulated emission from the edge of the plasma and consecutive inward shells. Mathematically, the inversion method is described by the following equation:

$$\varepsilon_{qp}(r) = -\frac{1}{\pi}\int_r^R \frac{\mathrm{d}L_{qp}(y)}{\mathrm{d}y}\frac{\mathrm{d}y}{\sqrt{y^2-r^2}} \tag{3.8}$$

3.5.2 A Fourier-based Abel inversion method

The implementation of the Abel inversion method that is used during this work [53], is Fourier-based and works slightly different [54]. The unknown radial profile is approximated by a series of cosine functions f_n that are all symmetric with respect to the centre of the plasma beam:

$$\hat{\varepsilon}_{qp}(r) = \sum_n A_n f_n(r) \tag{3.9}$$

in which the amplitude A_n of each cosine-component is unknown and in which the cosine-functions are given by:

$$f_0(r) = 1 \qquad f_n(r) = 1 - (-1)^n \cos\left(n\pi\frac{r}{R}\right) \tag{3.10}$$

The advantage of using this cosine expansion is that a forward Abel transform (see equation 3.7) can easily be carried out. The resulting profile $\hat{L}_{qp}(y)$ can be used to approximate

the measured LOS-profile $L_{qp}(y)$, using the amplitudes A_n as fitting parameters during a least squares fitting method. By substituting the obtained values of A_n back into equation 3.9, the unknown radial profile $\varepsilon_{qp}(r)$ is obtained.

3.5.3 Concerning the line-of-sight profiles

Irrespectively of the Abel inversion method that is being used, the line-of-sight profiles need to satisfy the following criteria in order to obtain reliable emission coefficient profiles $\varepsilon_{qp}(r)$:

- **Cylindrical symmetry**
  Equations 3.7 and 3.8, which form the core of both Abel inversion methods, are derived based on the assumption that the radiating plasma is cylindrically symmetric. An immediate consequence of this assumption is that the LOS-profiles $L_{qp}(y)$ also need to be symmetric with respect to the centre of the plasma beam. In practice, this is often not the case for the measurements. This asymmetry could be attributed to an asymmetric plasma (camera images of the plasma beam show evidence of this being the case) or a possible misalignment of the fiber array with respect to the centre of the plasma beam. In order to correct for this asymmetry, the position of the centre of the beam needs to be determined, after which the right and left side can be averaged to obtain symmetric LOS-profiles.
- **Extrapolation at the edges**
  The geometry of the Abel inversion also requires that the line radiance drops to a value close to zero at the edge of measured LOS-profile. However, due of the limited number of lines-of-sight being used by the multi-chord spectrometer set-up, it is not always possible to observe the edges of the plasma, as a consequence of which the radiance at the boundary of the LOS-profiles has not yet dropped to zero. The Abel inversion methods will attribute this offset to a localised radiation source at the surface of the plasma, making the Abel inverted profile $\varepsilon_{qp}(r)$ unreliable for radial positions outside the centre of the plasma beam. Instead, an extrapolation method can be used to force the LOS-signal to fall off to zero at large distances from the centre of the emission profile.
- **A smooth line-of-sight profile**
  Most Abel inversion methods are quite sensitive to fluctuations in the input data, because they distort the derivative $\mathrm{d}L_{qp}(y)/\mathrm{d}y$ that is being used to calculate the radial profiles and, therefore, lead to inaccurate results. Smoothing the LOS-profiles before the Abel inversion either by filtering out noise, having an higher sample rate or by using external smoothing routines, should yield better Abel inverted results.

  The Fourier-based Abel inversion has another method to deal with these irregularities, making this method less sensitive to fluctuations in the input data. By reducing the amount of terms in the cosine-expansion (see equations 3.9 and 3.10), the Abel inversion method limits the flexibility of the radial profile, effectively rendering it unable to follow any fast fluctuations when obtaining the amplitudes A_n during the fitting step. As a consequence, the effect of the irregular input data on the Abel inverted profile is reduced, but this also makes it possible that some physical details of the LOS-profile are being neglected.

An easy way to satisfy all these criteria is to approximate the measured LOS-profiles with a smooth and continuously defined fitting function that is symmetric with respect to the origin and that falls off to zero at its edges. The first candidate is the single Gauss as described by equation 2.21. Although commonly used, this function does not have enough free fitting parameters to capture the behaviour of the profile when it slightly departs from the precise Gaussian shape and, therefore, is not suitable.

The second candidate uses two exponential functions to describe a general peak shape [26]:

$$f(x) = A\Big(1 - \frac{1}{1+\exp((x-x_1)/dx)} - \frac{1}{1+\exp(-(x-x_2)/dx)}\Big) \tag{3.11}$$

in which A is the amplitude of the peak, dx indicates the width of the peak and x_1 and x_2 are the positions of both exponentials. By changing dx as well as the positions of both exponentials with respect to each other, the function can be used to describe a variety of peaks, including triangularly shaped peaks, Gaussian-like peaks and peaks with a flat top. As such, this function works quite good as a general approximation of the profile shape, but it does not accurately resolve the details at the centre of the plasma beam.

A more sophisticated fitting function that is based on the shape of the observed emission profiles, uses a combination of three Gaussian functions. The first Gaussian has a relatively large width to account for the wings of the LOS-profile, the second Gaussian resolves the bulk of the peak and the third Gaussian is inverted and takes care of the flat or hollow top of the profile [16, 47]. The described fitting function has the following shape:

$$f(x) = A_1 \exp\Big[-\Big(\frac{x-x_0}{dx_1}\Big)^2\Big] + A_2 \exp\Big[-\Big(\frac{x-x_0}{dx_2}\Big)^2\Big] + A_3 \exp\Big[-\Big(\frac{x-x_0}{dx_3}\Big)^2\Big] \tag{3.12}$$

in which x_0 indicates the central position of the peak. The amplitude of the different Gaussian components satisfy $A_2 > A_1 > 0$ and $A_3 < 0$, while the widths satisfy $dx_1 > dx_2 > dx_3$.

Using this fitting function, all main characteristics of the measured LOS-profiles can be captured in a smooth and symmetric approximation, which can subsequently be used as an input to either of the two Abel inversion methods to obtain the desired radial emission coefficient profiles $\varepsilon_{qp}(r)$.

3.6 Summary

The multi-chord spectrometer system that has been developed and installed on Magnum-PSI during this project and which is described in paragraph 3.1, is a flexible and powerful diagnostic tool. The procedure that is needed to interpret its measurements, however, is quite complex. Therefore, the data analysis chain that has been developed for this purpose, has been explained in detail in this chapter.

Crucial steps in this analysis chain are the determination of the location of the different fibers and the wavelength calibration (see paragraph 3.2.1) and the Labsphere intensity calibration (see paragraph 3.2.2). Especially the intensity calibration, which converts camera counts into actual spectral radiances, is essential when determining the excited state population densities, as is one of the goals mentioned in paragraph 1.8. The importance of a good spectral fitting routine and Abel inversion method have already been stressed in paragraph

2.7. As discussed in paragraph 3.3, instrumental line broadening is the dominant line broadening mechanism which results in spectral lines with a width of approximately 2.2 nm. This is taken into account while carrying out the spectral fitting procedure (see paragraph 3.4, which enables the determination of the total lines radiances L_{qp} using equation 3.6. Finally, the Abel inversion method described by equation 3.9 can be used to obtain the emission coefficients that are key in determining the excited state densities, as stated in paragraph 2.7.

Chapter 4

Spectroscopy and detachment experiments in Magnum-PSI

This chapter describes the detachment-experiments that were carried out in Magnum-PSI in order to answer the research questions as posed in paragraph 1.8. The Thomson scattering and multi-chord spectroscopy measurements that were taken during these experiments at different stages during the onset of detachment, will be discussed, focusing on the characterisation of detachment in Magnum-PSI and on investigating which processes are dominant at each stage of the onset of detachment.

4.1 Hydrogen injection and detachment in Magnum-PSI

In chapter 3, a method to determine radial emission coefficient profiles $\varepsilon_{qp}(r)$ based on spectroscopic measurements using multiple lines-of-sight through the plasma has been presented. In this chapter, the described method is used to study the emission of Balmer lines during detachment experiments in Magnum-PSI using the recently installed Jarrell-Ash multi-chord spectrometer (see paragraph 3.1).

During the experiments, spectroscopic measurements have been carried out at different neutral background pressures, in order to investigate the onset of detachment at an increasing neutral density in the target chamber of Magnum-PSI. For that purpose, it is important that the neutral background pressure in the target chamber can be controlled by adjusting the injection rate of molecular hydrogen into the target chamber with respect to the constant pumping speed of the vacuum pumps. Additionally, the effect of recycling could be investigated by either having a target in close proximity of the measurement position (at 3 cm) or retracted to a distance of 10 cm from the measurement position, assuming that the plasma flow in the target chamber is fully developed, i.e. the flow of the plasma is not affected by distance from the source anymore.

A steady-state attached plasma has been taken as the starting scenario for the experiments. In this scenario, the magnetic field of the superconducting magnet was set to 1.2 T, the gas flow through the cascaded arc source was 4 slm (standard liter per minute), the cathode current in the plasma source was kept at 120 A and the vacuum pumps were used

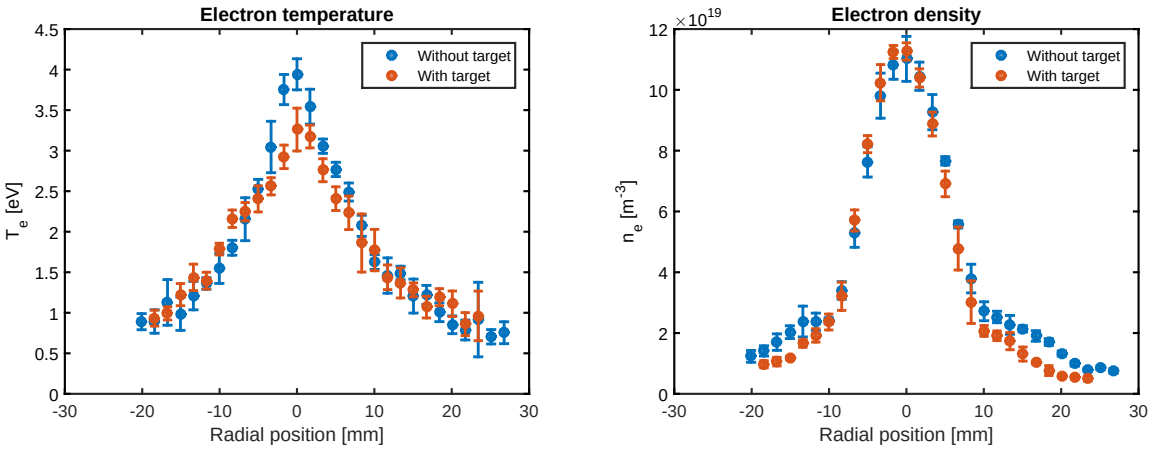

(a) The electron temperature.

(b) The electron density.

Figure 4.1: Electron temperature and electron density profiles for the starting scenario as measured by the Thomson scattering system.

at 100 % pumping speed. The purpose of choosing these conditions was to obtain demanding divertor-relevant plasma conditions that are difficult to detach, i.e. relatively high electron temperatures ($T_e \approx 3.5$ eV) and densities ($n_e \approx 10^{20}$ m^{-3}), while keeping the neutral background pressure inside the target as low as possible ($p_{bg} = 0.27$ Pa). The corresponding T_e and n_e profiles were measured by the Thomson scattering system (TS) [27] and the results are shown in figure 4.1. As can be seen, the electron temperature in the centre of the plasma beam is lower when a target is present near the measurement position. This drop in temperature can be attributed to the effect of recycling at the target: neutrals enter the main plasma at the target due to recombination, which subsequently extract energy from the plasma when they are re-ionised or dissociated.

Figure 4.2 shows a number of images that were taken by the fast Phantom camera (equipped with a H-α bandpass filter), while slowly increasing the background pressure from the starting scenario to $p_{bg} \approx 16.5$ Pa. Since the temperature in the attached starting scenario (a) is quite high (above 3 eV according to figure 4.1a), the main (left) part of the

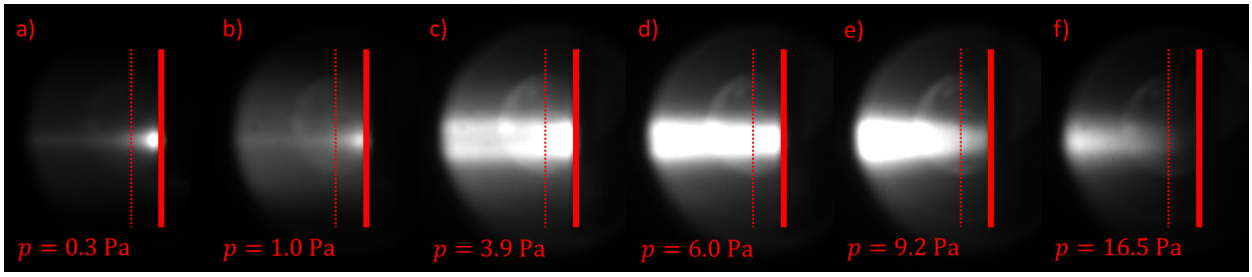

Figure 4.2: The onset of detachment with increasing background pressure in Magnum-PSI, as captured by the Phantom camera using a H-α bandpass filter. The thick solid line indicates the position of the target and the dotted line indicates the measurement position of the TS system as well as the multi-chord spectrometer.

plasma will be almost fully ionised according to equation 2.37. Consequently, most of the (H-α) radiation is emitted in close proximity to the target as a consequence of the excitation of recycled particles due to direct electron impact. After injecting some neutral hydrogen in the target chamber (b), the neutrals in the background start to emit a significant amount of radiation too after they get excited by the plasma. By increasing the neutral background pressure even further (c) and (d), the plasma cools down rapidly, subsequently causing molecular-assisted recombination (MAR) and electron-ion recombination (EIR) to become important. As a result of this, a strongly radiating region develops in front of the target at the position where the recombined particles are excited by the plasma. This radiating region expands in the upstream direction as the plasma cools down further with increasing background pressure. Eventually (e) and (f), the plasma detaches from the wall, effectively extinguishing in a region close to the target. In this detached region, no excitation occurs and, as such, there is no light emitted near the target.

In order to quantify the effect of the hydrogen injection, the electron temperature T_e and electron density n_e were monitored using the Thomson scattering system. As can be seen in figure 4.3a, the temperature drops rapidly with increasing p_{bg}. As described in paragraphs 1.3 and 1.4, this is the result of the interactions between the plasma and the neutral background particles. The processes that are responsible for the dissipation of energy are, consecutively, ionisation, charge-exchange reactions (CX), MAR and EIR. Figure 4.3b shows that the electron density initially increases with increasing background pressure. After reaching a maximum at around $p_{bg} \approx 4$ Pa, the electron density starts to decrease again. The behaviour at low background pressures is the direct result of the ionisation process which acts as a source for electrons at the Thomson scattering location and further upstream. As the background pressure increases, the amount of present neutrals increases and, consequently, more ionisation reactions take place. At even higher pressures, the temperature drops, making recombination processes (MAR and EIR) dominant. These processes are a sink for electrons and, as such, the electron density decreases for these conditions [55].

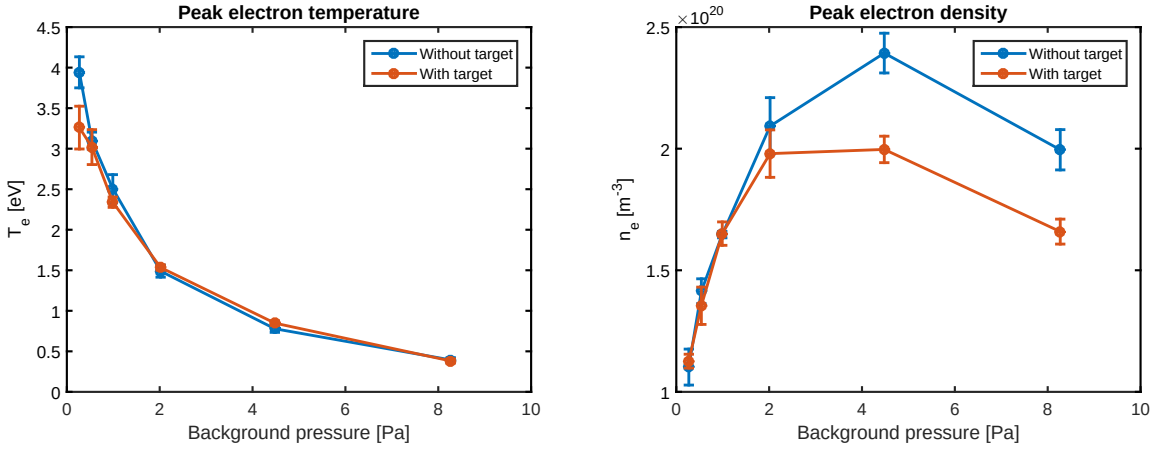

(a) The electron temperature.

(b) The electron density.

Figure 4.3: The peak electron temperature and electron density as function of the neutral background pressure as measured by the Thomson scattering system.

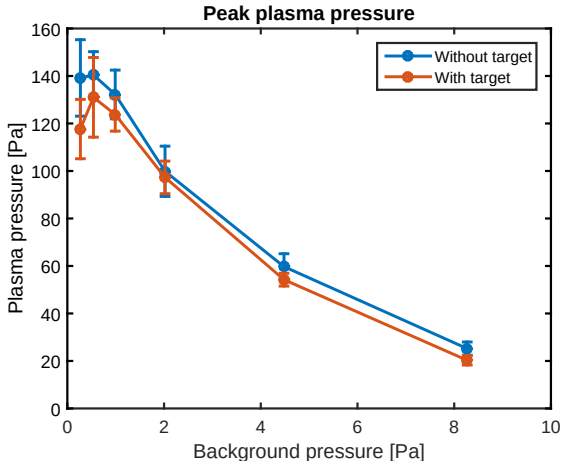

Figure 4.4: The measured peak plasma pressure as function of the neutral background pressure based on TS measurements. The decreasing plasma pressure is characteristic for plasma detachment.

When a target is in close proximity of the Thomson scattering position, recycling is expected to have an influence on the measured T_e and n_e. As explained before, ionisation is the dominant plasma process at low background pressures. Since ionisation removes energy from the plasma particles, the temperature should be lower when recycling is taken into account, which is also in agreement with figure 4.3a. The density is expected to be higher, since the ionisation of neutrals acts as an extra source of ions and electrons, but this cannot be seen in figure 4.3b. In the recombining regimes, the effect of recycling on the temperature is negligible, because the low temperature prohibits efficient ionisation of the recycled neutrals. The large difference in electron density at higher background pressures, on the other hand, can be explained by the fact that the increased neutral density due to recycling helps in extinguishing the plasma faster, leading to a lower electron density. This effect is not observed at low background pressures, because the recycled neutrals are ionised instead.

Assuming that $T_i = T_e$ and $n_i = n_e$, it is possible to calculate the plasma pressure P at each value of the background pressure p_{bg} based on the Thomson scattering measurements in figure 4.3: $P = 2n_e k_b T_e$. As can be seen in figure 4.4, the plasma pressure drops with increasing p_{bg}. Assuming that the upstream plasma conditions do not change, i.e. all changes take place due to the high background pressure in or just before the target chamber, this indicates that some of the plasma pressure is lost along the magnetic field lines, which is, as mentioned in paragraph 1.4, a key characteristic of plasma detachment [17].

4.2 Optical emission spectroscopy

In addition to the previously discussed Thomson scattering measurements, multi-chord spectroscopy has been carried out in order to investigate the population density of the excited states corresponding to the Balmer transitions H-β ($n = 4$) to H-θ ($n = 10$). The results of these measurements will be discussed in the next paragraphs.

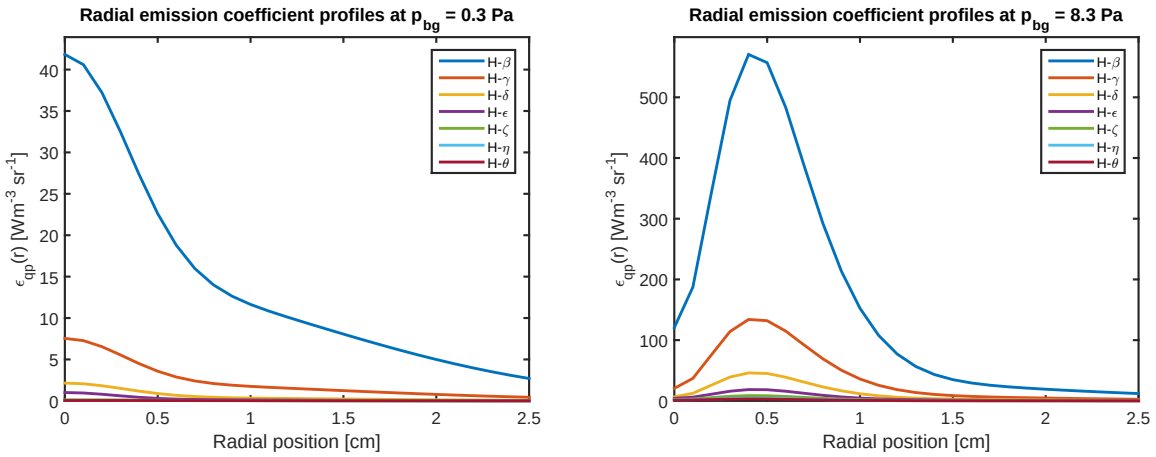

(a) Background pressure of 0.3 Pa.

(b) Background pressure of 8.3 Pa.

Figure 4.5: The measured radial emission coefficient profiles $\varepsilon_{qp}(r)$ for the different Balmer transitions at two different background pressures. Beware of the different scales on the y-axes. The measurements were taken in the presence of a target.

Figure 4.5 shows the measured radial emission coefficient profiles $\varepsilon_{qp}(r)$ obtained after using an Abel inversion for the different Balmer transitions at two different background pressures. Comparing the different transitions for a given pressure, it is clearly visible that the emission coefficients decrease for subsequent Balmer transitions, which is also in agreement with what is shown in figure 3.5a. This behaviour is also expected based on equation 2.3, because the Einstein coefficients for spontaneous emission A decreases for subsequent lines [31], while at the same time, the excited state population density n_q also decreases, because more energy is required to excite particles to subsequent energy levels (see equation 2.9).

From the radial emission coefficient profiles $\varepsilon_{qp}(r)$, it is relatively straight-forward to obtain the excited state population profiles $n_q(r)$ using equation 2.3. The resulting density profiles are shown in figure 4.6 and look rather similar to the radial emission coefficient profiles that have been shown before.

More interestingly, the figure also illustrates how the radial excited state density profiles change with respect to the neutral background pressure. As can be seen in figure 4.6a, the densities are relatively small in the attached case ($p_{bg} \approx 0.3$ Pa). This is also conform the expectations based on figure 4.2 and has two main reasons: most particles inside the plasma beam will be ionised, because the temperature is still relatively high (see figure 4.3a), and, secondly, the availability of (neutral) particles in general is relatively low at a low background pressures. The excited particles at the centre of the beam ($r = 0$ cm) are either coming from the target, as recycled neutrals are excited by collisions with the plasma, or from the plasma source itself. Towards the edge of the beam, the excited state densities decrease, because there are less plasma particles that can cause the excitation. However, the ionisation degree decreases simultaneously due to the significant drop in T_e and n_e towards the edge (see figure 4.1). Consequently, the excited state densities at the edge of the plasma do not decrease as rapidly as the decreasing electron density. Figure 4.7 shows that the excited states are less populated when no recycling takes place, i.e. when the target is far away from the

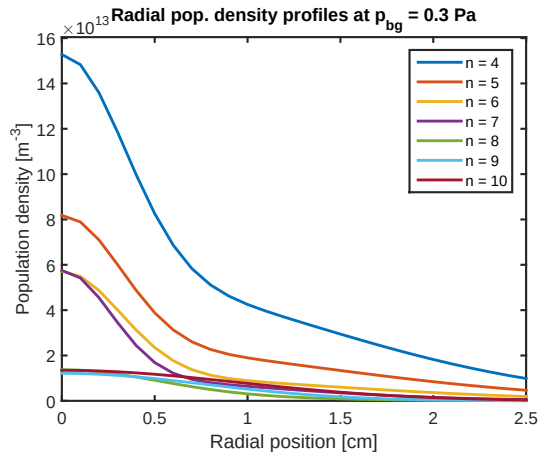

(a) Background pressure of 0.3 Pa.

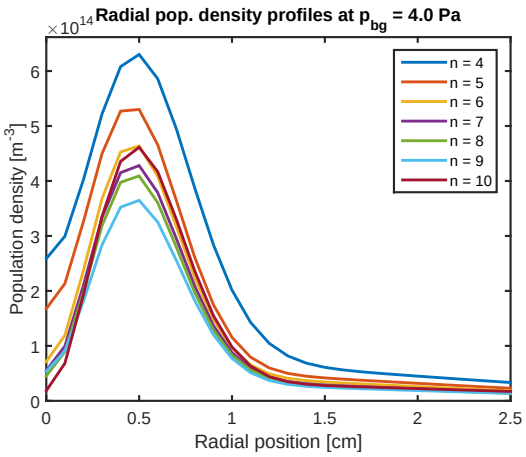

(b) Background pressure of 4.0 Pa.

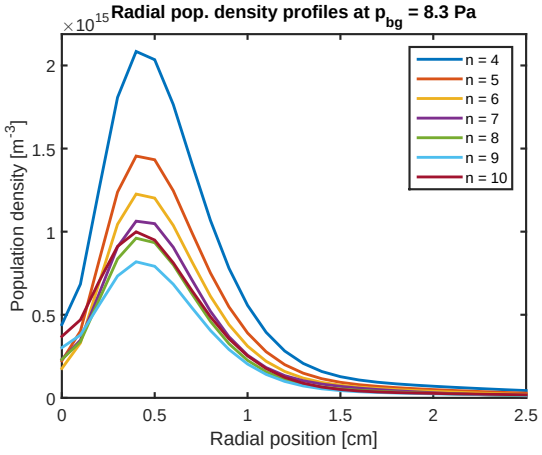

(c) Background pressure of 8.3 Pa.

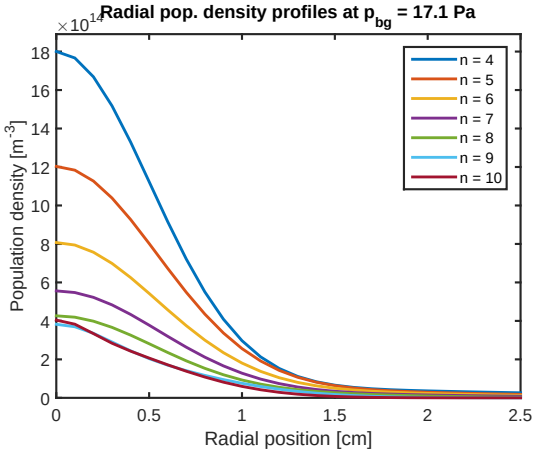

(d) Background pressure of 17.1 Pa.

Figure 4.6: The measured radial excited state population density profiles $n_q(r)$ for the different Balmer transitions at different background pressures. Beware of the different scales on the y-axes. The measurements were taken in the presence of a target.

measurement position (dashed line). During the recycling process, recombination at the wall produces atomic neutrals and vibrationally excited molecules. Subsequently, molecular dissociation and electron impact excitation mainly populate the lower excited states, as is observed in figure 4.7.

When the background pressure is raised to $p_{bg} \approx 4.0$ Pa, a strongly radiating region starts to develop at the measurement position (also shown in figure 4.2), which results in an enormous increase in the amount of measured radiation coming from the plasma and, consequently, higher excited state population densities. Due to the higher background pressure, the temperature drops below $T_e \approx 2$ eV (see figure 4.3a), which is the threshold at which MAR processes start to play a role according to figure 1.6. The characteristic hollowness of the radial density profiles can be explained by considering where MAR processes are most effective, i.e. where the product of the electron density and the density of hydrogen molecules $n_e \cdot n_{H_2}$ is highest [47]. This is not the case in the core of the plasma beam,

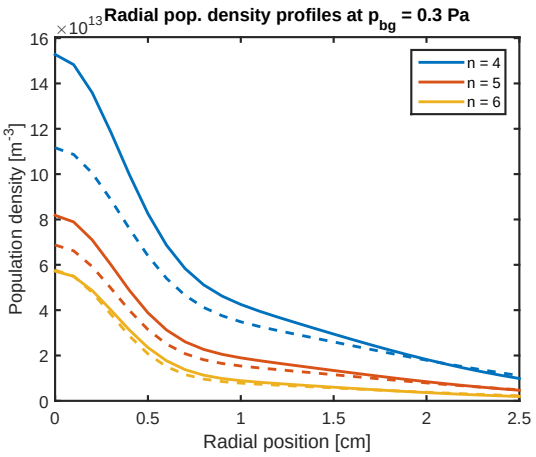

Figure 4.7: Measured $n_q(r)$ profiles at a background pressure of 0.3 Pa with (solid line) and without (dashed line) the presence of a target close to measurement position.

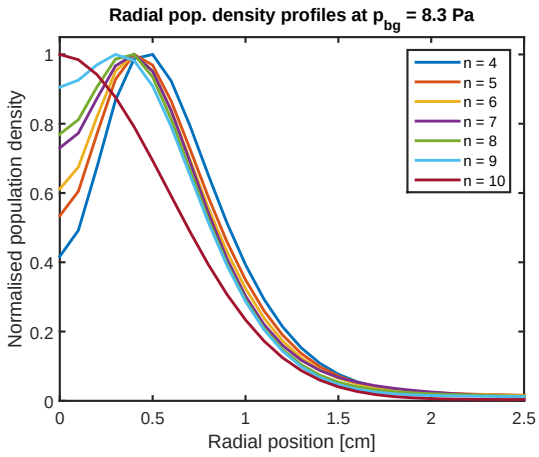

Figure 4.8: Measured $n_q(r)$ with a background pressure of 8.3 Pa and without the presence of a target.

since the H_2-particles which are injected during the experiment to increase the background pressure, are pushed away from the core by the plasma pressure. At $r \approx 0.5$ cm, which is just outside the core, the H_2-density can be much higher. In addition, the electron density, which is a peaked profile, is also still relatively high, guaranteeing the perfect conditions for MAR to play an important role. The production of excited neutrals during MAR reaction (either due to dissociative recombination of H_2^+ or due to molecular mutual recombination, see table 1.1) and the subsequent excitation of these particles to even higher energy levels by the electrons in the plasma beam, lead to the observed peaks in the excited state densities, as can be seen in figure 4.6b. At larger radial distances, the electron density drops further (see figure 4.1b), again reducing the effect of the MAR and excitation processes.

As shown in figure 4.2, the recombination region expands in an upstream direction when the background pressure is increased to $p_{bg} \approx 8.3$ Pa. Consequently, the observed radiation is emitted from deeper inside the recombination region, leading to increasingly higher population densities, as can be seen in figure 4.6c. The measurements shown in figure 4.6 were taken with a target in close proximity of the measurement position. Figure 4.8 shows similar, albeit normalised, measurements that were taken without the presence of a target. As can be seen, the hollowness of the density profiles becomes less prominent and it even vanishes completely for H-θ. This effect can be attributed to EIR, which acts as a source for highly excited hydrogen atoms according to table 1.1 if the temperature is lower than 0.5 eV (see figure 1.6). EIR is most effective in the core of the plasma, because the electron density n_e is highest in this region. Figure 4.6c does not show any significant signs of this EIR-induced behaviour, since the electron density is much smaller in the case where a target is present, as can be seen in figure 4.3b.

Figure 4.6d, finally, shows the radial excited state population density profiles for the detached scenario ($p_{bg} \approx 17.1$ Pa). In this case, the profiles are almost entirely dominated by EIR as the main production mechanism for excited hydrogen atoms and all signs of hollowness have disappeared. The decreasing temperature at the core makes the EIR process more

efficient as can be seen figure 1.6 and, as such, the observed excited state densities increase. At the same time, however, the electron density decreases while the plasma extinguishes, as can be seen in figure 4.3b, eventually again reducing the effect of EIR and, subsequently, the excited state densities for even higher pressures.

4.3 Investigating (p)LTE

In order to compare the population densities of the different excited states, $\ln(n_p/g_p)$ is plotted as function of the energy difference $E_p - E_g$ using the Boltzmann plot method, as described in paragraph 2.5.

Figure 4.9 shows a Boltzmann plot for the attached baseline scenario ($p_{bg} \approx 0.27$ Pa) measured in the core of the plasma bundle, i.e. at a radial position of $r = 0.0$ cm. The Boltzmann plot seems to indicate that the upper two excited states are in pLTE, since they are populated according to the Boltzmann distribution corresponding to the T_e that has been measured by the Thomson scattering system. To verify this behaviour, the population of higher excited states need to be measured, which has not been possible with the current spectrometer set-up. Additionally, the Boltzmann plot shows an overpopulation of the lower excited states which is, as discussed in paragraph 2.5, characteristic for ionising plasmas. This is in agreement with previous measurements, because both the measured radial OES profiles (see figure 4.5a) together with the relatively high electron temperature (see figure 4.1a) suggest that ionisation is the dominant plasma process that takes place in this specific scenario.

At higher background pressures, Boltzmann plots behave differently, since other processes are responsible for the population of the different excited states. For the $p_{bg} \approx 8.3$ Pa case, for instance, MAR is expected to be the dominating processes, as has been argued in paragraph 4.2. Because MAR mainly populates the $n = 2 - 4$ states (see equations 1.2 and 1.3 and

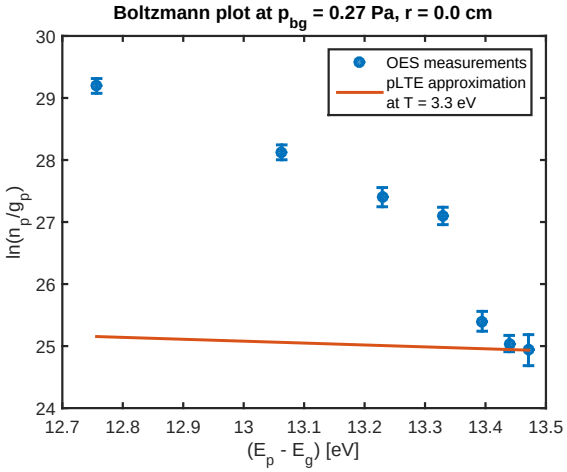

Figure 4.9: Boltzmann plots for the attached baseline scenario, illustrating the behaviour of the excited state population distribution in an ionising plasma. The pLTE approximated distribution (red line) is based on Thomson scattering measurements of the electron temperature.

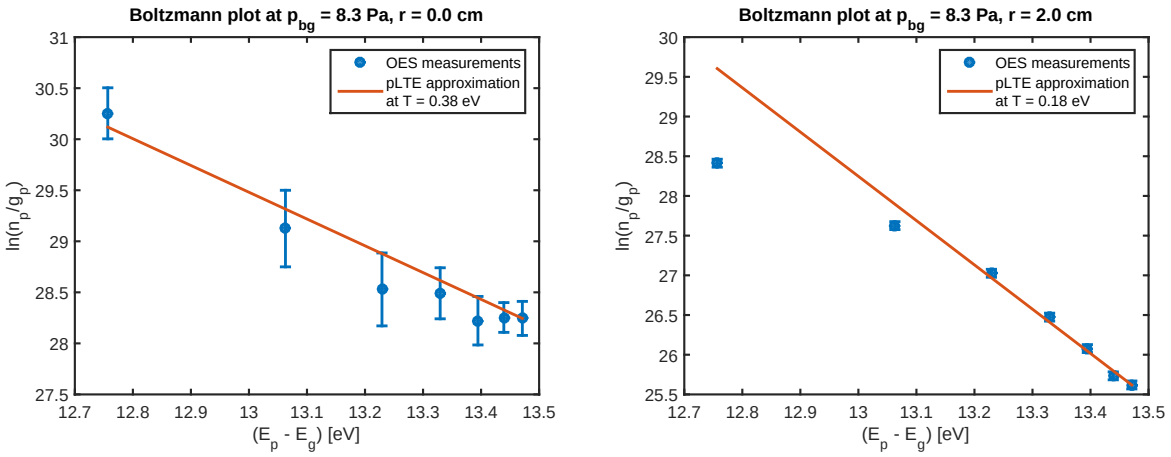

(a) Measured at $r = 0.0$ cm.

(b) Measured at $r = 2.0$ cm.

Figure 4.10: Boltzmann plots for the slightly detached scenario ($p_{bg} \approx 8.3$ Pa), illustrating the behaviour of the excited state population distribution in a recombining plasma. The pLTE approximated distribution (red line) is based on Thomson scattering measurements of the electron temperature.

table 1.1) instead of the higher excited states, the underpopulation of the lower excited states, which is characteristic for recombining plasmas, cannot be seen in figure 4.10a. However, when looking at a radial position more towards the outside of the plasma beam, e.g. at $r = 2.0$ cm, the temperature has dropped below 0.3 eV and, as such, EIR is the dominant recombination process, as can be seen from the reaction rates in figure 1.6. Figure 4.10b shows the corresponding Boltzmann plot, which indicates that the states $n \leq 6$ are populated according to pLTE, whereas the upper excited states are underpopulated, as is expected for recombining plasmas.

In the fully detached case with a background pressure of $p_{bg} \approx 17.3$ Pa (see figure 4.11),

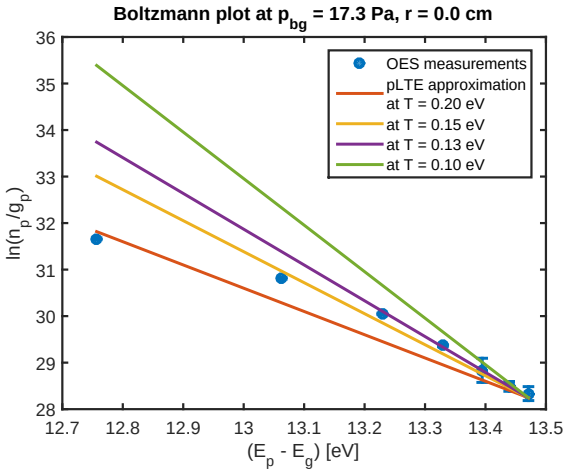

Figure 4.11: Boltzmann plots for a fully detached scenario, illustrating the behaviour of the excited state population distribution in an ionising plasma.

EIR also becomes the dominant process at the centre of the plasma beam and, as such, the excited states are similarly populated as the ones shown in figure 4.10b: underpopulation of the lower excited states and the upper excited states are populated according to pLTE. However, it is difficult to verify whether the upper excited states are actually in pLTE, because Thomson scattering could not provide an accurate electron temperature measurement in these conditions. The reason for this is that it was impossible to distinguish the actual TS signal from the measured spectrum, because the width of the TS signal, which scales with T_e, was of the same order as the instrument function, meaning that the electron temperature for the detached conditions was simply too low to be measured. However, assuming that pLTE is satisfied for the upper excited states, which would be expected based on figure 4.10, the Boltzmann plot method makes it possible to determine the electron temperature purely based on the spectroscopic measurements. As can be seen in figure 4.11, the electron temperature T_e is estimated to be approximately 0.13 eV. Even though this estimation cannot be verified using Thomson scattering measurements, a temperature of 0.13 eV would make sense with respect to the trend shown in figure 4.3a.

4.4 Summary

In paragraph 4.1, it has been shown that raising the neutral background pressure leads to a major reduction in the electron temperature. Moreover, the electron density decreases at high background pressures while the plasma extinguishes. A strongly radiating region has been observed at medium background pressures, indicating the presence of a recombination front and also the effect of recycling has been discussed. Spectroscopic measurements of the excited state densities in the form of radial profiles (see paragraph 4.2) and Boltzmann-plots (see paragraph 4.3), show that subsequently ionisation, molecular-assisted recombination and electron-ion recombination are the dominant plasma processes that are responsible for the observed experimental trends at increasing background pressures in Magnum-PSI. As such, these processes are also expected to play a role during the onset of detachment in tokamak divertors.

Chapter 5

Conclusion and outlook

Each of the research questions that were posed in paragraph 1.8, will be answered in this final chapter. Moreover, this chapter covers possibilities for follow-up work on the multi-chord spectrometer system, the detachment experiments on Magnum-PSI and the validation of Yacora as a CR-model for MANTIS.

5.1 Conclusion

During the experiments carried out in Magnum-PSI the background pressure has been gradually increased by actively seeding hydrogen into the vacuum vessel. While doing so, Thomson scattering measurements that were taken at increasingly high background pressures, show decreasing electron temperatures and densities, indicating a drop in plasma pressure. Additionally, fast camera images show a strongly radiating region developing in front of the target, due to the ionisation and subsequent recombination of recycled neutrals or neutrals from the background gas. At increasing background pressures, this strongly radiating region expands in upstream direction, illustrating the presence of a recombination front. The presence of a recombining region (with a recombination front) in which the plasma extinguishes, as indicated by the decreasing electron temperatures and densities, together with a characteristic drop in plasma pressure, prove that it is possible to achieve detachment in Magnum-PSI by controlling the neutral background pressure.

During this project, a Czerny-Turner multi-chord spectrometer system has been installed on Magnum-PSI to investigate the excited state densities during the detachment experiments. Due to its rotatable grating mount, the system is capable of scanning for different wavelengths and, as such, the system is capable of observing the Balmer lines up to H-θ, as well as numerous other impurity lines. By interchanging the grating, the system can be used to provide relatively wide overview spectra or high-resolution spectra of narrow spectral regions. More importantly, the system uses a fiber array consisting of 40 optical fibers which each measure the line-integrated emission of the plasma along it entire line-of-sight. Exploiting the different fibers, a spatial resolution of 1.1 mm can be achieved with the current configuration of the viewing system. Using a subsequent Abel inversion, local emission coefficients can be obtained from the line-integrated signals and, as such, also radial excited state density profiles can be measured. Hence, the new multi-chord spectrometer system is a flexible and

powerful tool to study the light emitted by the plasma in Magnum-PSI during detachment experiments and in general.

As mentioned before, the multi-chord spectrometer has been used to observe the emitted light at different stages during the onset of detachment, i.e. at different background pressures. The resulting radial emission profiles and the corresponding Boltzmann-plots, combined with the information about the plasma parameters (T_e and n_e) and the reaction rates of the different plasma processes, make it possible to draw conclusions about the processes that are responsible for the population of the excited states. In the attached baseline scenario, where the temperature is still fairly high, ionisation is the dominant processes, as indicated by a peaked emission profile and the overpopulation of the lower excited states. At higher background pressures, the temperature has dropped and the hollowness of the emission profiles show that molecular-assisted recombination becomes important, especially at radial positions slightly away from the centre of the plasma beam, where the product of n_e and n_{H_2} is highest. At even higher pressures, the plasma effectively detaches and electron-ion recombination is responsible for the population of the excited states, as indicated by a peaked emission profile and the underpopulation of the lower excited states.

5.2 Outlook

This paragraph discusses a number of possibilities which can be explored to continue this work. These can typically be divided into the following three categories:

- **Improving the multi-chord spectrometer set-up**
  The well-established Avantes spectrometer system that is being used during most experiments in Magnum-PSI, is only capable of providing spectral information for a single line-of-sight with a pre-determined spectral resolution in a number of pre-determined spectral regions. Consequently, a flexible spectrometer that provides spatially resolved spectral information, such as the multi-chord spectrometer used during this project, could be a very interesting addition to Magnum's standard inventory of diagnostics. However, in the case of the current multi-chord spectrometer set-up, this would require several upgrades to improve its reliability and user-friendliness. These improvements include:
  - **The system that rotates the grating** is currently controlled by manually turning the switch at the set-up itself. The improved set-up should be able to rotate the grating precisely and automatically to a desired wavelength as specified from within the control room. Additionally, a new wavelength axis should be automatically defined for each new grating orientation. Both adjustments require the new set-up to compensate for the hysteresis which currently affects the rotation mechanism. The main advantage of this is that it becomes possible to investigate multiple spectral lines during the same experiment, for instance, H-α could have been included in the measurements presented in chapter 4 relatively easily.
  - **The internal alignment** of the current set-up is decent, but not optimal, since the set-up consist of different components that are put together. Improving the

alignment can easily be achieved when it becomes possible to adjust the positioning of the entrance fiber, the slit and the camera more precisely with respect to each other. An improved alignment would allow a narrower slit and, therefore, a higher spectral resolution. The mirrors and grating holder inside the spectrometer can be adjusted accordingly. This would enable the investigation of spectral line shapes and the subsequent determination of T_e and n_e based on these measurements. Additionally, this would be beneficial for molecular spectroscopy (more about this elsewhere in this paragraph).

- **Reducing the light throughput** is often necessary to prevent overexposure of the current CCD-array, especially when looking at highly radiating regions. During this project it was possible to include several neutral density filters into the set-up by placing them in front of the camera. In the future, the throughput of light could be controlled remotely by using an aperture or a filter wheel. Having this option, makes the spectrometer suitable for use in highly radiating scenarios. Additionally, since H-α is brighter than the other lines, measuring this line also requires some way of dealing with the relatively high intensity.
- **The grating holder** needs to be removed from within the spectrometer to change gratings which affects the internal optical alignment of the spectrometer. Consequently, it would be useful to design a grating holder which does not suffer from this issue. Alternatively, a grating holder could be designed which holds multiple gratings at once, eliminating the need to take the grating holder out of the spectrometer to swap gratings.
- **Integration of the system** to Magnum's main control and data-storage system allows other people to operate the diagnostic. This also gives the opportunity to make standard data-analysis software which can be used by anyone.

- **Experimental work on detachment in Magnum-PSI**
  Even though detachment in linear machines differs from detachment in actual tokamaks, due to the milder starting conditions, the smaller connection lengths and the absence of a core that can be influenced by whatever happens in the SOL, experiments in linear machines can be used to investigate the processes that are responsible for the onset of detachment in divertor-relevant plasma conditions. In this context, the advantages of linear machines are their simplicity, which makes it easier to compare experiments and simulations, their possibility of having steady-state operation and their diagnostic acces. Follow-up research of detachment in Magnum-PSI could focus on the following topics:

  - **The ionisation to MAR transition** is expected to occur at a neutral background pressure of $p_{bg} \approx 2$ Pa when using the same machine parameters as used during this project. Unfortunately, the spectroscopy results were overexposed and, as such, this transitions could not be observed accurately. Revisiting this scenario could explain how the hollow emission profiles develop.
  - **Investigating higher Balmer lines** and determining the population densities of the higher excited states, would enable a better interpretation of the Boltzmann-plots. Since the higher excited states are expected to be in pLTE, this would also make it easier to investigate whether the lower excited states are overpopulated

(ionising plasma) or underpopulated (recombining plasma) with respect to pLTE. This, however, requires an updated spectrometer with a higher spectral resolution.
  - **Measurements at different axial positions** along the beam, in addition to the radial profiles, could provide information about the length scales that are involved with the movements of the different fronts that appear during the onset of detachment.
  - **A spectroscopic analysis of molecular bands** could provide more information about the population of the vibrational levels, which are critical for MAR processes, and the influence of H_2 on the onset of detachment. Moreover, this opens up the possibility of determining the ground-state density of molecular hydrogen (see appendix A).
  - **Other detachment-related topics**, such as nitrogen seeding and detachment in ELMy plasmas, have not been discussed in this work, but are also being investigated in Magnum-PSI. In the case of nitrogen seeding, which is considered to be one of the primary seeding gasses for tokamaks, the plasma chemistry is more extensive and, as such, also the processes that are responsible for the detachment could be different. Multi-chord spectroscopy could play an important role in determining which process is dominant at each stages during the onset of detachment, similar as has been done during this project. Using time-resolved multi-chord spectroscopy, it is possible to investigate how a sudden heat pulse (and the subsequent relaxation) influences the importance of the different plasma processes, in the case of ELMy plasmas.

- **Validation of the Yacora CR-model**
  Finally, the excited state population densities that were measured during this project can contribute to the validation of the Yacora CR-model, when the measured densities are compared with their calculated values based on Yacora. However, the complete validation can only be carried out when the ground-state densities of the previously mentioned atomic and molecular hydrogen species are known, because these are necessary to calculate the excited state densities. The experimental determination of these ground-state densities, therefore, is an absolute must before Yacora can be used as a tool to interpret MANTIS measurements.
  After the validation, Yacora can be used to generate a database-like tool that relates measured line ratios to actual plasma parameters (T_e and n_e). Using this tool, MANTIS can be used to investigate the temperature and density of the divertor plasmas in tokamaks in a two-dimensional and time-resolved while the plasma detaches. Additionally, MANTIS can also be used during normal operation to obtain the plasma parameter, as well as during instabilities like ELMs and MARFEs.

Appendix A

Molecular line emission and Fulcher band spectroscopy

As mentioned in paragraph 2.1, molecules are also partially responsible for the emission of line radiation due to bound-bound transitions. Therefore, this appendix deals with the energy level structure of molecules, focusing on di-atomic molecules and in particular on molecular hydrogen H_2 and the Fulcher band transitions. Moreover, uncalibrated spectroscopic measurements will be presented and, finally, it will be discussed how calibrated measurements can be used to investigate the influence of H_2.

A.1 Molecular energy level structure

Similar as is the case for atoms (see equation 2.11), the electronic states of a molecule can be characterised by term symbols. These molecular term symbols are generally written in the following form:

$$n^{(2S+1)}\Lambda_{(g/u)}^{(+/-)} \tag{A.1}$$

in which n indicates the electronic state using an empirical notation: X denotes the ground state and subsequent states are indicated by letters in alphabetical order. Capital letters (A, B, C, ...) are used for singlet states ($S = 0$), whereas lower-case letters (a, b, c, ...) are used for triplets ($S = 1$). The symbol S denotes the total electron spin of the molecule, i.e. the sum of the spin of the individual electrons in the unfilled energy levels. Λ, indicated by Greek letters (Σ, Π, Δ, ...), denotes the total orbital angular momentum projected along the internuclear axis. Finally, $+$ or $-$ denotes the symmetry of the electron distribution molecule with respect to the internuclear axis and u or g denotes the parity of the molecule, which is the symmetry of the electron distribution with respect to the centre of mass of the molecule [30].

In molecules, the exact energy of an electronic state is a function of the internuclear distance R. At large distances, the potential energy of the molecule is relatively high, due to the attractive forces between each nucleus and the electron that is circling around the other nucleus. At very short distances, the potential energy increases very quickly, because of the repulsive forces between both nuclei and both electrons. Somewhere in the middle, when R

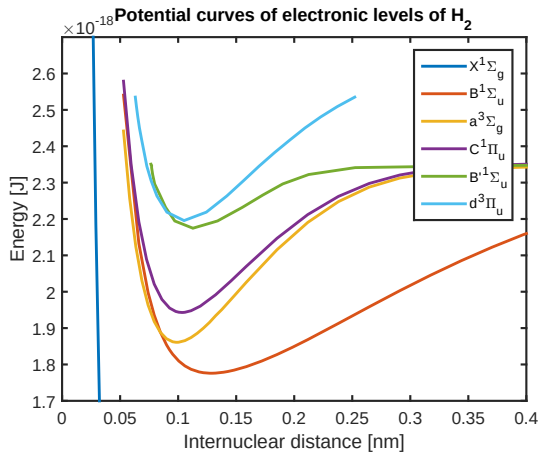

Figure A.1: The electronic energy curves of the hydrogen molecule H_2, showing the different electronic states [56]. Electronic transitions between the $d^3\Pi_u^-$-state and the $a^3\Sigma_g^+$-state result in the emission of light in the so-called Fulcher Band, which will be discussed in further detail in section A.2.

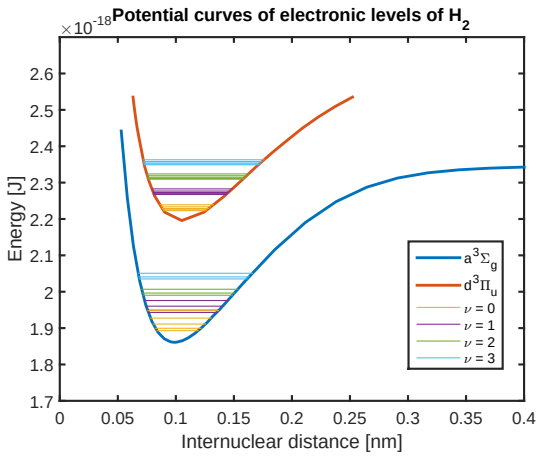

Figure A.2: The potential curves of the electronic energy levels that make up the Fulcher-α transitions. The figure also shows the first ro-vibrational levels contained in both electronic energy levels [57]. Subsequent levels are in order of increasing ν (different color) and J (same color).

equals the equilibrium distance R_e, the energy levels have a minimum, as is shown in figure A.1 for the hydrogen molecule. Finally, the molecule dissociates at $R \to \infty$, releasing the binding energy at which the potential curve levels off.

Although the electronic energy levels are most prominent, the energy level structure of (diatomic) molecules is characterised by a large number of vibrational and rotational levels that are contained within each electronic structure. In addition to the molecular term symbol that indicates the electronic state of the molecule, an energy level is now characterised by a vibrational quantum number ν and a rotational quantum number J. The energetic spacing between vibrational levels is smaller than the spacing between electronic levels, but larger than the spacing between rotational levels, as can be seen in figure A.2.

A.2 The Fulcher band

A spectral feature that is commonly observed in the visible part of spectrum (590 - 640 nm) of molecular hydrogen H_2 is the so-called Fulcher-α band. This band consists of a large number of closely spaced spectral lines which all have in common that they originate from the same electronic transition, namely the transition: $d^3\Pi_u^- \to a^3\Sigma_g^+$. The different peaks are a consequence of different ro-vibrational transitions within the aforementioned electronic transition. Electronic and ro-vibrational energy levels that correspond to the Fulcher-α band, are shown in figure A.2.

In the (partially) detached scenarios that were described in chapter 4, the neutral H_2 background pressure is very high and, as a consequence, the Fulcher-α band can easily be observed. Moreover, using a relatively long integration time (several minutes), the Fulcher

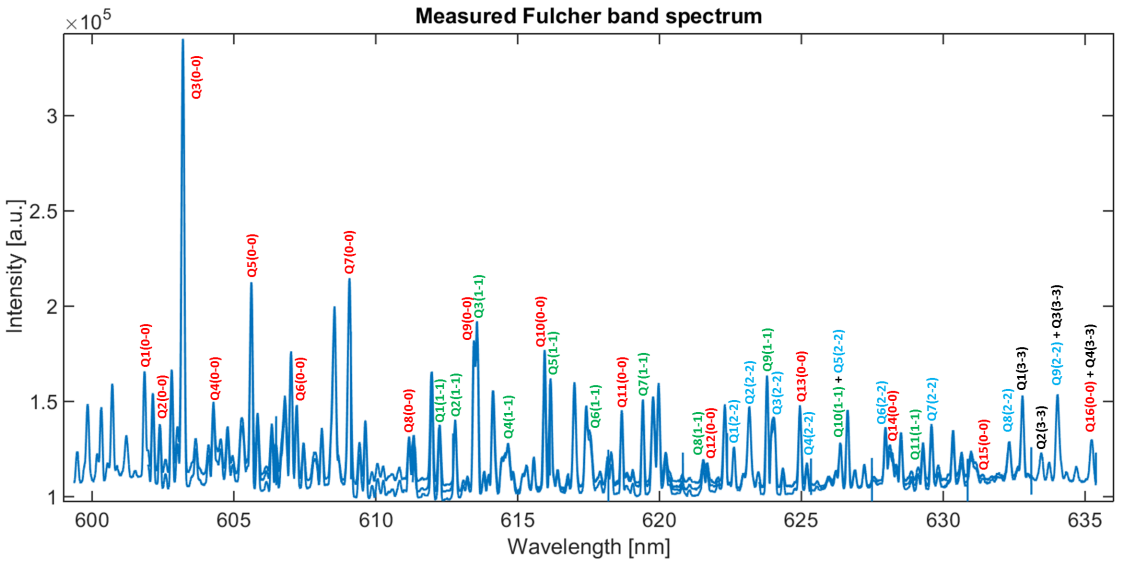

Figure A.3: An uncalibrated composite spectrum of the Fulcher band as measured in Magnum-PSI at a neutral background of $p_{bg} \approx 0.5$ Pa. All Q-branch transitions are labeled based on their vibrational transition (indicated by the color and the numbers between the brackets) and the rotational transition (the number in front).

band has been measured even at background pressures as low as $p_{bg} \approx 0.5$ Pa, as can be seen in figure A.3. Note that for these measurements the spectrometer has been equipped with the high-resolution grating (see table 3.1) in order to resolve the different peaks. In order to reach a background pressure of 0.5 Pa during these measurements, the operational parameters were set to be as follows: a magnetic field of 0.8 T, a gas flow of 5 slm, a cathode current of 120 A and 25 % pumping speed in the target chamber.

As can be seen in figure A.3, multiple diagonal vibrational bands can be observed, consisting of spectral peaks that are the result of purely rotational transitions, i.e. transitions during which the vibrational quantum number does not change ($\nu' = \nu''$). Each individual peak is therefore characterised by its rotational transition: the Q-branch consists of lines corresponding to transitions in which the rotational quantum number does not change ($J' = J''$) either, whereas the rotational off-diagonal P-branch and R-branch correspond to transitions in which $\Delta J = +1$ or $\Delta J = -1$, respectively. As such, the $Q3(1-1)$-peak indicates a transition between the following levels $(\nu, J) = (1, 3) \rightarrow (1, 3)$, which is a purely electronic transition, and the $R5(3-2)$-peak indicates the ro-vibrational off-diagonal transition between $(\nu, J) = (3, 5) \rightarrow (2, 4)$.

Figure A.4 shows two section of the Fulcher band spectrum in which, in addition to the Q-branch, also the P- and R-branches are labeled. Moreover, the spectrum contains ro-vibrational off-diagonal transitions and spectral peaks that cannot be described by Fulcher band transitions. These lines correspond to different electronic transitions, which can be identified using wavelength tables [58]. Overlap with these peaks can distort the Fulcher band lines, as is, for instance, the case for the $Q3(0-0)$-line [59]. The measured peak positions correspond nicely to the expectations [60], but the relative peak intensities are different, due to the missing calibration and, more importantly, the different plasma conditions.

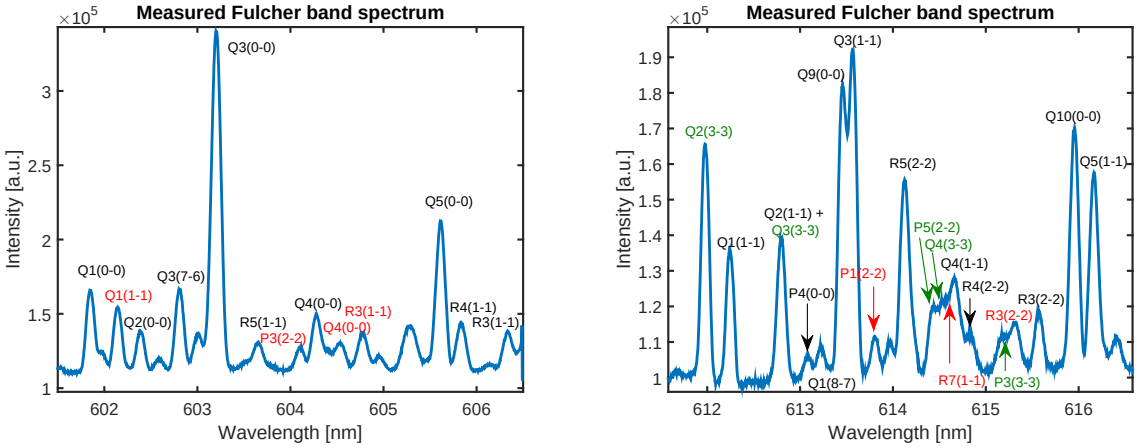

(a) Fulcher band region for wavelengths between 601.5 - 606.5 nm.

(b) Fulcher band region for wavelengths between 612.5 - 616.5 nm.

Figure A.4: Two sections of the Fulcher band spectrum containing spectral lines that are the result of actual Fulcher band transitions (labeled in black) as well as spectral lines that find their origin in a different electronic transition. The lines that are labeled in red are emitted due to an electronic transition from the $g^3\Sigma_g^+$-state to the $c^3\Pi_u^-$-state and the green labeled lines are the result of a $i^3\Pi_g^- \rightarrow c^3\Pi_u^-$-transition.

A.3 Investigating the effect of H_2

Based on the measured Fulcher-α band spectrum, it is possible to define a rotational temperature of H_2 for each diagonal vibrational band using a Boltzmann plot in a similar way as has been done in paragraph 4.3. Assuming that all levels are populated according to the Boltzmann distribution, the total band brightness ε_M can be estimated, while taking an extra factor of 2 into account to compensate for the P- and R-branches that are not measured explicitly [61]. For this purpose, the diagonal vibrational transitions are considered mainly because they are the strongest, while the non-diagonal transitions are take into account by using an extra branching ratio. When the total band brightness is known, the H_2 flux towards the target Γ_M can be obtained using:

$$\Gamma_M = \frac{4\pi}{h\nu}\varepsilon_M \frac{D}{XB} \tag{A.2}$$

in which D is the total decay rate of molecules in the upper Fulcher band state due to dissociation and ionisation processes, X is the excitation rate and B is the branching ratio. The D/XB factor has been experimentally determined in calibration experiments (at a given combination of plasma parameters), as well as via CR modeling [62].

In addition to that, the measured Fulcher band emission can sometimes be used to estimate the H_2 ground-state densities. For low electron densities, CR calculations have shown that the ratio between the emission coefficients of the Fulcher band and H-γ transition are almost independent of T_e and only slightly dependent on n_e. In these conditions, the ratio $\varepsilon_{H_\gamma}/\varepsilon_M$ gives a decent indication of the density ratio n_H/n_{H_2} [60, 63].

Bibliography

[1] International Energy Agency, *World Energy Outlook 2015 Factsheet*

[2] S. Shafiee and E. Topal, *When will fossil fuel reserves be diminished?*, Energy Pol., Vol. 37, Nr. 1 (2009)

[3] J. Freidberg, *Plasma physics and fusion energy*, Cambridge University Press (2007)

[4] S. Atzeni and J. Meyer-ter-Vehn, *The physics of inertial fusion*, Oxford Science Publications (2009)

[5] J. Wesson, *Tokamaks*, 3th edition, Oxford Science Publications (2004).

[6] J.R. Gilleland et al., *ITER: Concept definition*, Nucl. Fusion, Vol. 29, Nr. 7 (1989)

[7] P.C. Stangeby, *The plasma boundary of magnetic fusion devices*, Taylor & Francis Group, London (2000)

[8] M. de Baar et al., *A strategy to address exhaust issues in the EU Fusion programme*, Report of the STAC Ad Hoc Group (2013)

[9] D.M. Duffy, *Fusion power: a challenge for materials science*, Phil. Trans. R. Soc. A, Vol. 368 (2010)

[10] H. Zohm et al., *On the physics guidelines for a tokamak DEMO*, Nucl. Fusion, Vol. 53, Nr. 7 (2013)

[11] B.A. Lomanowski, *Visible and near-infrared divertor spectroscopy on the MAST and JET-ILW tokamaks*, PhD Thesis, Durham University (2015)

[12] S.I. Krasheninnikov, *Divertor plasma detachment*, Phys. Plasmas, Vol. 23, Nr. 5 (2016)

[13] The iso-nuclear master files from the ADF11 class on the open version of the atomic data and analysis structure, `http://open.adas.ac.uk/`, version 2.0, OPEN-ADAS [accessed on: 28-06-2017]

[14] A.S. Kukushkin et al., *Role of molecular effects in divertor plasma recombination*, Nucl. Mater. Energy (2017)

[15] R.K. Janev et al., *Collision processes in low-temperature hydrogen plasmas*, Berichte des Forschungszentrums Jülich, Vol. 4105, (2003).

[16] W.J. van Harskamp, *Plasma chemistry and kinetics in a magnetized hydrogen plasma expansion*, PhD Thesis, Eindhoven University of Technology (2012)

[17] G.F. Matthews, *Plasma detachment from divertor targets and limiters*, J. Nucl. Mater., Vol. 220-222 (1995)

[18] J.R. Harrison, *Characterisation of detached plasmas on the MAST tokamak*, PhD Thesis, University of York (2010)

[19] The plasma edge physics and diagnostic group of the Dutch institute for fundamental energy research, `https://www.differ.nl/research/pepd`, DIFFER [accessed on: 18-03-2017]

[20] J.R. Harrison et al., *Detachment evolution on the TCV tokamak*, Nucl. Mater. Energy (2016)

[21] S.H.M. van Limpt, *Development of a 2D multi-spectral imaging technique to measure T_e and n_e in divertor plasmas*, MSc Thesis, Eindhoven University of Technology (2016)

[22] D. Wünderlich, *Berechnung von Teilchendichten für die Diagnostik an Niedertemperaturplasmen*, PhD Thesis, University of Augsburg (2004)

[23] D. Wünderlich, S. Dietrich and U. Fantz, *Application of a collisional radiative model to atomic hydrogen for diagnostic purposes*, J. Quant. Spectrosc. Ra., Vol. 110, Nr. 1-2 (2009)

[24] N. Ohno, *Plasma detachment in linear devices*, Plasma Phys. Contr. F., Vol. 59, Nr. 3 (2017)

[25] H.J.N. van Eck, *The linear plasma generator Magnum-PSI*, PhD Thesis, Eindhoven University of Technology (2013)

[26] W.A.J. Vijvers, *A high-flux cascaded arc hydrogen plasma source*, PhD Thesis, Eindhoven University of Technology (2011)

[27] H.J. van der Meiden et al., *Advanced Thomson scattering system for high-flux linear plasma generator*, Rev. Sci. Instrum., Vol. 83, Nr. 12 (2012)

[28] G. Pretzler, *A new method for numerical Abel-inversion*, Z. Naturforsch. A, Vol. 46, Nr. 7 (1991)

[29] H.-J. Kunze, *Introduction to plasma spectroscopy*, Springer-Verlag Berlin Heidelberg (2009)

[30] W. Demtröder, *Atoms, molecules and photons*, 2nd edition, Springer-Verlag Berlin Heidelberg (2010)

[31] NIST atomic spectra database, `http://physics.nist.gov/asd`, version 5, National Institute of Standards and Technology, Gaithersburg [accessed on: 10-04-2017]

[32] H. Skenderovic and V. Vujnovic, *A study of the line broadening constants obtained in a high-pressure mercury discharge*, J. Quant. Spectrosc. Ra., Vol. 55, Nr. 2 (1996)

[33] N. Konjevic, *Plasma broadening and shifting of non-hydrogenic spectral lines: present status and applications*, Phys. Rep., Vol. 316, Nr. 6 (1999)

[34] A.W. Ali and H.R. Griem, *Theory of resonance broadening of spectral lines by atom-atom impacts*, Phys. Rev. 140, Nr. 4A (1965) and the revision in Phys. Rev. 144, Nr. 1 (1966).

[35] I.I. Sobel'man, L.A. Vainshtein and E.A. Yukov, *Excitation of atoms and broadening of spectral lines*, 2nd edition, Springer series on atoms and plasmas (1995)

[36] P. Thompson, D.E. Cox and J.B. Hastings, *Rietveld refinement of Debye-Scherrer synchrotron X-ray data from Al_2O_3*, J. Appl. Cryst., Vol. 20, Nr. 2 (1987)

[37] H.A. Kramers, *On the theory of X-ray absorption and of the continuous X-ray spectrum*, Phil. Mag., Vol. 46, Nr. 275 (1923)

[38] E.A. Milne, *Statistical equilibrium in relation to the photo-electric effect, and its application to the determination of absorption coefficients*, Phil. Mag., Vol. 47, Nr. 277 (1924)

[39] J.A. Gaunt, *Continuous absorption*, Phil. Trans. R. Soc. A, Vol. 229 (1930)

[40] W.J. Karzas and R. Latter, *Electron radiative transitions in a coulomb field*, Astrophys. J. Suppl. S., Vol. 6 (1961)

[41] H.R. Griem, *Principles of plasma spectroscopy*, Cambridge University Press (1997)

[42] J.A.M. van der Mullen, *Excitation equilibria in plasmas; a classification*, Phys. Rep., Vol. 191, Nr. 2-3 (1990)

[43] D. Lumma, J.L. Terry and B. Lipschultz, *Radiative and three-body recombination in the Alcator C-Mod divertor*, Phys. Plasmas, Vol. 4, Nr. 7 (1997)

[44] C. Palmer and E. Loewen, *Diffraction grating handbook*, 6th edition, Newport Corporation (2005)

[45] Princeton Instruments imaging group, *Datasheet - PIXIS: 2048*, Rev. 5.1 (2014)

[46] Labsphere Inc., *Halogen Light Sources*, Rev. 13 and *Single Illuminator US-Series Integrating Spheres*, Rev. 0

[47] A.E. Shumack, *The influence of electric fields and neutral particles on the plasma sheath at ITER divertor conditions*, PhD Thesis, Eindhoven University of Technology (2011)

[48] S.P. Goldman, *Gauge-invariance method for accurate atomic-physics calculations: Application to relativistic polarizabilities*, Phys. Rev. A, Vol. 39, Nr. 3 (1989)

[49] P. Schwerdtfeger, *Table of experimental and calculated static dipole polarizabilities for the electronic ground states of the neutral elements*, Center for Theoretical Chemistry and Physics, Auckland (2015)

[50] H.C. Goldwire, *Oscillator strengths for electric dipole transitions of hydrogen*, Astrophys. J. Suppl. S., Vol. 17, Nr. 125 (1968)

[51] Maxim, *Peak fitting to either Voigt or LogNormal line shapes*, `https://mathworks.com/matlabcentral/fileexchange/52321`, Version 1.1, MATLAB file exchange [accessed on: 24-04-2017]

[52] J. Glasser, J. Chapelle and J.C. Boettner, *Abel inversion applied to plasma spectroscopy: a new interactive method*, Appl. Optics, Vol. 17, Nr. 23 (1978)

[53] Carsten Killer, *Abel Inversion Algorithm*, `https://mathworks.com/matlabcentral/fileexchange/43639`, Version 1.5, MATLAB file exchange [accessed on: 10-05-2017]

[54] G. Pretzler, *A new method for numerical Abel-inversion*, Z. Naturforsch. A, Vol. 46, Nr. 7 (1991)

[55] Y. Hayashi et al., *Plasma flow in peripheral region of detached plasma in linear plasma device*, Phys. Plasmas, Vol. 23, Nr. 1 (2016)

[56] T.E. Sharp, *Potential-energy curves for molecular hydrogen and its ions*, Atomic Data and Nuclear Data Tables, Vol. 2 (1971)

[57] G.H. Dieke, *The Molecular Spectrum of Hydrogen and Its Isotopes*, J. Mol. Spectrosc., Vol. 2 (1958)

[58] H.M. Crosswhite, *The hydrogen molecule wavelength tables of Gerhard Heinrich Dieke*, Whiley-interscience (1972)

[59] N. den Harder et al., *Residual gas entering high density hydrogen plasma: rarefaction due to rapid heating*, Plasma Sources Sci. T., Vol. 24, Nr. 2 (2015)

[60] J.J. Dang, K.J. Chung and Y.S. Hwang, *A simple spectroscopic method to determine the degree of dissociation in hydrogen plasmas with wide-range spectrometer*, Rev. Sci. Instrum., Vol. 87, Nr. 5 (2016)

[61] E.M. Hollmann et al., *Spectroscopic measurement of atomic and molecular deuterium fluxes in the DIII-D plasma edge*, Plasma Phys. Control. Fusion, Vol. 48, Nr. 8 (2006)

[62] S. Brezinsek et al., *On the measurement of molecular particle fluxes in fusion boundary plasmas*, J. Nucl. Mater., Vol. 313-316 (2003)

[63] U. Fantz et al., *Spectroscopy - a powerful diagnostic tool in source development*, Nucl. Fusion, Vol. 46, Nr. 6 (2006)